Digest Journal of Nanomaterials and Biostructures

Dig. J. Nanomater. Bios. **2026**; 21(2): 55237
https://doi.org/10.31083/DJNB55237

Original Research

Advanced Biopolymer-Based Zn-Co-Fe/Ca Nanocomposites for High-Performance Dye Removal From Aqueous Media

Shaju Pragash Maria John[1], Jayganesh Duraipandian[2,*]

[1]Department of Civil Engineering, Ponjesly College of Engineering, 629003 Nagercoil, India
[2]Department of Civil Engineering, Anna University Regional Campus, 625019 Madurai, India
*Correspondence: jayganeshd2003@gmail.com (Jayganesh Duraipandian)
Academic Editor: Maria Harja
Submitted: 14 December 2025 Revised: 3 March 2026 Accepted: 11 March 2026 Published: 24 June 2026

Abstract

Due to the toxicity, persistence, and high visibility of synthetic dyes, the discharge of dye-contaminated effluents from textile and allied industries represents a major environmental concern. This study reports the development of a sustainable, high-performance biopolymer-based nanocomposite incorporating zinc, cobalt, iron, and calcium (Zn-Co-Fe/Ca) to overcome the limitations of conventional adsorbents. The primary objective was to evaluate the adsorption efficiency and mechanistic behaviour of the developed adsorbent for methylene blue (MB) removal from aqueous media. The biopolymer-based Zn-Co-Fe/Ca nanocomposite, hereafter referred to as Biopolymer-based Zn-Co-Fe/Ca Magnetic Nanocomposite (BPMNC), was synthesised via chemical co-precipitation followed by ionic crosslinking within a calcium alginate matrix. Comprehensive physicochemical characterisation using scanning electron microscopy (SEM), Fourier transform infrared (FTIR) spectroscopy, X-ray diffraction (XRD), X-ray photoelectron spectroscopy (XPS), Brunauer–Emmett–Teller (BET) surface area analysis, thermogravimetric analysis (TGA), and point of zero charge (pH_pzc) confirmed effective metal immobilisation, mesoporous surface characteristics, and strong dye–surface interactions. Batch adsorption experiments were conducted in triplicate (n = 3) by varying pH (3–10), adsorbent dosage (0.5–2.5 g), contact time (10–90 min), initial MB concentration (4–20 mg L^{-1}), and temperature (30–70 °C). Adsorption kinetics and equilibrium behaviour were analysed using pseudo-first-order and pseudo-second-order models, along with Langmuir and Freundlich isotherms. Thermodynamic parameters (ΔG^0, ΔH^0, and ΔS^0) were determined using Van't Hoff analysis. At pH 6, an adsorbent dose of 1.0 g and an initial dye concentration of 12 mg L^{-1} with a contact time of 60 min resulted in a maximum MB removal efficiency of approximately 97%. The pseudo-second-order model 1 provided the best fit to the experimental data, with high correlation coefficients (R^2 = 0.9614–0.9808). Among the investigated concentrations, only the 20 mg L^{-1} system exhibited an R^2 value exceeding 0.98, while the remaining concentrations showed R^2 values between 0.96 and 0.98, indicating that the adsorption kinetics were generally well described by the pseudo-second-order model. The Langmuir isotherm (R^2 = 0.99) suggested monolayer adsorption on a homogeneous surface. SEM and FTIR analyses further confirmed significant dye–surface interactions, and thermodynamic results indicated a spontaneous and endothermic adsorption process. Consequently, the biopolymer-based adsorbent demonstrated high and stable MB removal at near-neutral pH due to synergistic multi-metal interactions and surface functionalities, highlighting its potential as a sustainable adsorbent for dye-laden wastewater treatment.

Keywords: adsorption efficiency; biopolymer-based adsorbent; methylene blue removal; wastewater treatment; Zn-Co-Fe/Ca nanocomposite

1. Introduction

The industrial discharge of synthetic dye-contaminated wastewater poses a significant global environmental challenge due to the high toxicity, complex aromatic structures, and strong resistance of these compounds to biodegradation processes, which adversely affect both aquatic ecosystems and human health [1,2,3,4,5,6,7,8,9]. Among these dyes, methylene blue (MB) has been extensively investigated owing to its widespread industrial application and persistence in aqueous environments [10,11,12,13,14]. Conventional wastewater treatment techniques, including coagulation, flocculation, and biological degradation, often fail to achieve complete MB removal because of its stable molecular structure and low biodegradability, thereby necessitating the development of more efficient remediation strategies [15,16].

Adsorption is widely recognised as an effective technique for dye removal due to its operational simplicity, flexibility, and selectivity towards target pollutants [17]. Although activated carbon exhibits excellent adsorption capacity, its high cost, limited regeneration potential, and reduced selectivity restrict large-scale application [18]. Consequently, recent research has focused on eco-friendly biopolymer-based adsorbents, which facilitate dye removal through electrostatic attraction, hydrogen bonding, and ion-exchange mechanisms [19,20]. Natural biopolymers, such as sodium alginate and chitosan, provide renewable and biodegradable matrices enriched with functional groups that are favourable for dye binding [21,22,23]. Fur-

thermore, the incorporation of metal oxide nanoparticles within biopolymer frameworks significantly enhances adsorption capacity, mechanical stability, and structural integrity [24,25,26,27,28,29,30,31,32]. Recent studies have also reported the efficient photocatalytic degradation of dyes using nanocomposite systems, such as TiO_2/ZrO_2 and $CuOZrO_2$, highlighting the role of nanostructured materials in improving wastewater remediation performance [33,34]. In addition, several studies emphasise the growing importance of sustainable natural polymer-based bioadsorbents aligning with the United Nations Sustainable Development Goals (UN SDGs), and reinforcing the need for advanced and environmentally responsible research in dye wastewater treatment [23,32,35].

Despite these advances, the persistent release of chemically stable and toxic synthetic dyes such as MB from industrial effluents remains a major environmental concern due to their resistance to biodegradation and associated ecological and human health risks. To address the limitations of traditional adsorbents, such as high cost, limited reusability, and moderate adsorption efficiency, the present study reports the development of a Biopolymer-based Zn-Co-Fe/Ca Magnetic Nanocomposite (BPMNC) engineered to exploit synergistic physicochemical interactions within a sustainable calcium alginate matrix. In contrast to previously reported single- or binary-metal systems, the simultaneous incorporation of zinc, cobalt, and iron together with calcium enhances surface functionality, structural stability, and chemisorption-dominated dye uptake. Accordingly, this study systematically investigates the synthesis, characterisation, and adsorption behaviour of the developed biopolymer-based adsorbent, with a detailed evaluation of kinetic, isotherm, and thermodynamic responses to establish its potential as a high-efficiency and eco-friendly material for dye-contaminated wastewater treatment.

2. Materials and Methods

2.1 Materials and Chemicals

All chemicals and reagents used in the experimental work were of analytical grade (purity ≥99.9%) and were used without further purification. Cobalt(II) chloride ($CoCl_2$), iron(III) chloride ($FeCl_3$), zinc chloride ($ZnCl_2$), sodium hydroxide (NaOH), calcium chloride ($CaCl_2$), hydrochloric acid (HCl), and MB dye were procured from Merck India Ltd., Raigad 410203, Maharashtra, India. Sodium alginate biopolymer (purity ≥99.9%) was obtained from Loba Chemie Pvt. Ltd., Colaba, Mumbai 400005, Maharashtra, India. Deionised water was used throughout the synthesis and adsorption experiments to prevent interference from extraneous ions. Material selection was guided by compatibility with polymeric matrices and their established roles in adsorption-based wastewater treatment.

2.2 Synthesis of Zn-Co-Fe Ferrite Nanoparticles

Zn-Co-Fe ferrite nanoparticles were synthesised using a chemical co-precipitation method reported by Vaidyanathan and Sendhilnathan [36], with minor modifications. Briefly, Fe^{3+}, Co^{2+}, and Zn^{2+} salts were dissolved in 100 mL of double-distilled water at molar concentrations of 2.0 M, 0.5 M, and 0.5 M, respectively. The mixed metal salt solution was maintained at 60 °C under continuous magnetic stirring. The solution was rapidly added (within 10 s) to a boiling NaOH solution (pH ≈ 12), prepared by dissolving NaOH (0.63 M) in 1200 mL of deionised water. The reaction mixture was maintained at 85 °C for 1 h to facilitate the formation of spinel ferrite nanoparticles through hydroxide formation, dehydration, and atomic rearrangement. The resulting magnetic nanoparticles were separated using a high-strength permanent magnet, washed repeatedly with deionised water until a neutral pH was achieved, rinsed with acetone, and dried under ambient conditions.

2.3 Synthesis of the Biopolymer-Based Adsorbent

The biopolymer-based BPMNC was synthesised by dispersing Zn-Co-Fe ferrite nanoparticles within a sodium alginate matrix, followed by Ca^{2+}-induced ionic crosslinking using $CaCl_2$, as shown in Fig. 1. The synthesis was carried out through a systematic stepwise procedure to ensure uniform nanoparticle dispersion and effective crosslinking within the polymeric framework. A 1% (w/v) sodium alginate solution was prepared by dissolving the required amount of alginate in deionised water under continuous stirring until a homogeneous solution was obtained. Separately, 1 g of synthesised Zn-Co-Fe ferrite nanoparticles was dispersed in 5 mL of deionised water and ultrasonicated to achieve uniform dispersion. The nanoparticle suspension was subsequently mixed with the alginate solution and further ultrasonicated to obtain a stable composite suspension.

The resulting mixture was added dropwise using a syringe into a 100 mL solution of calcium chloride ($CaCl_2$) (0.5 M) under gentle stirring. Upon contact with Ca^{2+} ions, the alginate chains underwent ionic crosslinking, forming spherical Zn-Co-Fe ferrite–alginate composite beads. The beads were allowed to cure overnight to ensure complete gelation and structural stabilisation. The absence of colour in the residual calcium chloride solution indicated effective nanoparticle entrapment and negligible leaching. The beads were washed repeatedly with deionised water to remove unbound calcium ions and stored in double-distilled water until further use.

2.4 Characterisation Techniques

2.4.1 Fourier Transform Infrared (FTIR) Spectroscopy

FTIR spectroscopy (Model: ALPHA-II, Bruker Optics GmbH & Co. KG, Ettlingen, Baden-Württemberg, Germany) was employed to identify functional groups and chemical interactions within the nanocomposite over the range 400–4000 cm^{-1}. Characteristic absorption bands cor-

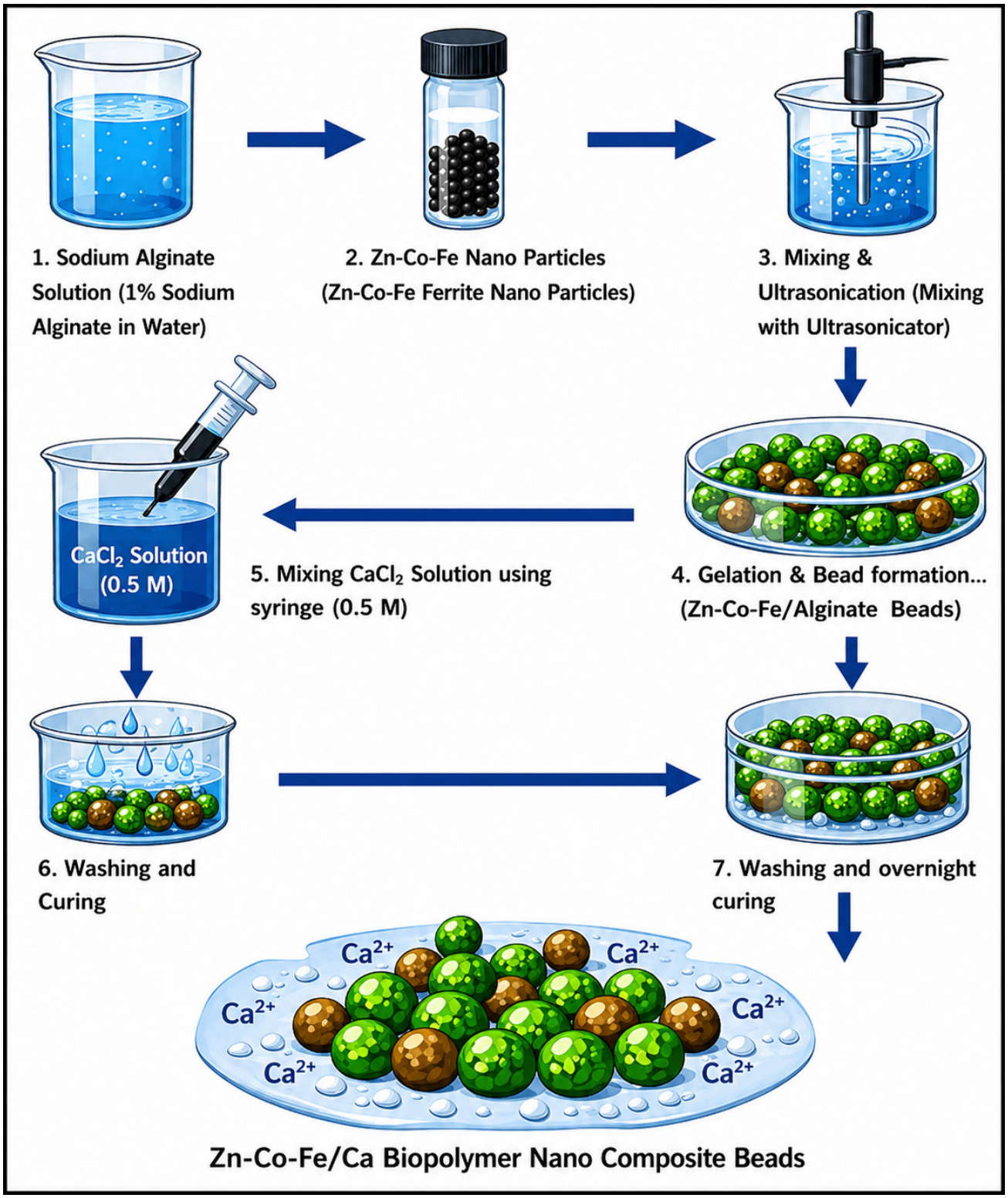

Fig. 1. Synthesis of BPMNC. BPMNC, Zn-Co-Fe/Ca nanocomposite.

responding to alginate functional groups and metal–oxygen bonds were observed. Shifts in peak positions and variations in band intensity confirmed interactions between the biopolymer matrix and metal components, which are essential for dye adsorption through electrostatic interactions and surface complexation.

2.4.2 X-ray Diffraction (XRD) Analysis

XRD analysis (Model: D8 ADVANCE, Bruker AXS GmbH, Karlsruhe, Baden-Württemberg, Germany) was performed to determine the crystalline structure, phase composition, and crystallinity of the nanocomposite. The

diffraction patterns confirmed the successful formation of mixed metal oxide phases embedded within the biopolymer matrix. Peak positions and intensities were analysed to evaluate structural order, phase purity, and crystallite size, which are critical parameters influencing adsorption performance.

2.4.3 X-ray Photoelectron Spectroscopy (XPS)

XPS (Model: K-Alpha, Thermo Fisher Scientific, East Grinstead, West Sussex, UK) was conducted to analyse surface elemental composition and oxidation states of Zn, Co, Fe, and Ca. The XPS spectra confirmed the presence of chemically active surfaces with multiple oxidation states. Binding energy analysis provided insight into surface chemistry and potential adsorption sites, enabling correlation between surface composition and adsorption behaviour.

2.4.4 Brunauer–Emmett–Teller (BET) Surface Area Analysis

BET surface area analysis (Model: ASAP 2020, Micromeritics Instrument Corporation, Norcross, GA, USA) was used to determine the specific surface area, pore volume, and pore size distribution of the nanocomposite. The material exhibited a predominantly mesoporous structure, facilitating dye diffusion and adsorption. The high surface area and suitable pore architecture contributed significantly to the adsorption efficiency.

2.4.5 Scanning Electron Microscopy (SEM)

SEM was used to examine surface morphology and microstructural features of the nanocomposite. SEM images (Model: VEGA3, TESCAN Group, Brno, South Moravian Region, Czech Republic) revealed a porous, heterogeneous surface with well-dispersed particles, favouring increased surface area and enhanced adsorption efficiency. The lack of significant particle agglomeration demonstrates successful synthesis and effective stabilisation of the composite framework.

2.4.6 Determination of the Point of Zero Charge (pH_pzc)

The pH_pzc (Model: SevenCompact S220, Mettler Toledo, Columbus, OH, USA) was determined to evaluate surface charge behaviour as a function of pH. This parameter is crucial for understanding electrostatic interactions between the adsorbent surface and dye species. The method involved monitoring pH changes in electrolyte solutions containing the nanocomposite, which enabled the interpretation of pH-dependent adsorption behaviour.

2.4.7 Thermogravimetric Analysis (TGA)

TGA (Model: TGA 550, TA Instruments, New Castle, DE, USA) was performed to evaluate the thermal stability and decomposition behaviour of the nanocomposite. The material demonstrated enhanced thermal resistance due to strong interactions between the polymeric matrix and metal oxides. Distinct weight-loss regions corresponded to moisture evaporation, organic decomposition, and structural stabilisation, confirming suitability for practical applications under varying thermal conditions.

2.5 Dye Adsorption Experiments

Batch adsorption experiments were conducted to evaluate MB removal using biopolymer-based adsorbent under varying conditions, including solution pH (3–10), contact time (10–90 min), temperature (30–70 °C), initial dye concentration (4–20 mg L^{-1}), and adsorbent dosage (0.5–2.5 g). Experiments were performed in 250 mL conical flasks containing 50 mL of dye solution, which were agitated at 300 rpm. Unless otherwise stated, experiments were conducted at room temperature using 1.0 g of the developed adsorbent. Solution pH was adjusted using 1 M HCl or NaOH. Following adsorption, the composite beads were magnetically separated, and residual dye concentration was determined using an Ultraviolet–visible spectrophotometer.

2.5.1 Preparation of Dye Solutions

Stock solutions of MB were prepared using deionised water, and working solutions were obtained by appropriate dilution. Strict control was maintained over solution preparation to ensure accurate concentrations and experimental reproducibility.

2.5.2 Batch Adsorption Studies

Batch adsorption studies were conducted to examine the effects of pH, contact time, adsorbent dosage, initial dye concentration, and temperature on adsorption performance. All experiments were conducted under controlled conditions until the adsorption equilibrium was established. The resulting data were used to evaluate adsorption efficiency and adsorption capacity.

2.5.3 UV–Visible Spectroscopic Analysis

Ultraviolet–Visible (UV–Vis) Spectroscopy (Model: UV–2202, Systronics India Ltd., Ahmedabad, Gujarat, India) was employed to quantify dye concentration before and after adsorption. The maximum absorption wavelength of methylene blue was used for all measurements, ensuring accurate assessment of removal efficiency and adsorption capacity. The corresponding UV–Vis absorption spectra, illustrating the spectral characteristics of the samples, are presented in **Supplementary Fig. 1**.

2.6 Reusability Studies

Reusability studies were performed to assess the regeneration capability and operational stability of the developed adsorbent over multiple adsorption-desorption cycles. After each cycle, the adsorbent was regenerated using suitable desorption agents, then thoroughly washed and reused. Adsorption efficiency was assessed after each cycle to de-

termine performance retention, demonstrating the practical applicability and sustainability of the biopolymer-based adsorbent.

3. Results

3.1 Structural and Phase Analysis of the Adsorbent Material

The structural, chemical, surface, and thermal properties of the biopolymer-based nanocomposite were systematically characterised using complementary analytical techniques to elucidate its suitability for adsorption applications. SEM provided insights into surface morphology and microstructural features, while XRD confirmed the crystalline phases present within the material. FTIR spectroscopy and XPS were employed to identify surface functional groups, bonding characteristics, and oxidation states of constituent elements. BET surface area analysis was used to determine specific surface area and porosity, which directly influence adsorption efficiency. Thermal stability and compositional behaviour were evaluated using TGA. Additionally, the pH_pzc was determined to assess surface charge characteristics and predict pH-dependent adsorption behaviour. Collectively, these characterisation techniques provide comprehensive insight into the structural integrity, surface chemistry, and adsorption potential of the developed adsorbent for environmental remediation applications.

3.1.1 FTIR Analysis

The FTIR spectra of the Biopolymer/Zn-Co-Fe and Biopolymer/Zn-Co-Fe-MB samples were compared to that of the Biopolymer/Zn-Co-Fe-Spent adsorbent to assess the changes in the material's structure after the adsorption process, as shown in Fig. 2. The spent adsorbent shows some noticeable differences in comparison to the fresh sample. There are small shifts in the peaks, particularly in the 3400 cm^{-1} region, which is often associated with O-H or N-H stretching, indicating that the interaction between the adsorbent and the MB dye may have caused slight changes in the molecular structure of the dye. Additionally, the intensity of the peaks in the spent sample is generally lower than in the fresh material, reflecting a reduction in the available surface for infrared (IR) absorption due to the adsorption of the dye. Some peaks may also be more prominent or slightly altered in the spent adsorbent spectrum, which suggests that the MB dye has interacted with the adsorbent's functional groups. Despite these changes, the overall structure of the spent adsorbent remains similar to that of the original Biopolymer/Zn-Co-Fe, with the alterations primarily indicating the successful adsorption of the MB dye.

3.1.2 XRD Analysis

Fig. 3 shows the XRD patterns for both the fresh and spent adsorbent samples. The blue solid line represents the fresh adsorbent, while the red dashed line shows the pattern for the spent adsorbent after the adsorption process. By comparing these two patterns, we can examine any changes in the material's structure after it has been used for adsorption.

In the XRD data, some shifts in the peaks were noticed between the fresh and spent samples. These shifts are important because they can indicate changes in the adsorbent's crystal structure. For example, if peaks move or change in height, it could mean that the adsorbent's structure has been altered during the adsorption process. Differences in peak intensities were also observed, indicating the extent of structural modification in the material. A drop in intensity may suggest a loss of crystallinity, while an increase could indicate the formation of new phases or material on the surface of the spent adsorbent.

Consequently, the XRD patterns for both the fresh and spent samples are quite similar, showing that the material's structure is mostly preserved. However, there are small differences in the intensities and positions of some peaks, which provide important insights into how the adsorbent behaves after use.

3.1.3 XPS Analysis

The XPS survey spectrum of the nanocomposite, as shown in Fig. 4, confirms the presence of Zn, Co, Fe, Ca, O, and C, verifying the successful incorporation of multimetal species within the biopolymer matrix. The intense C 1s and O 1s peaks originate from the alginate backbone, while distinct metal core-level signals confirm the formation of metal–oxygen coordinated structures. The C 1s spectrum exhibits peaks corresponding to C–C/C–H, C–O, and O–C=O functional groups, characteristic of alginate-based biopolymers and indicative of abundant oxygen-containing binding sites. The O 1s region shows contributions from lattice oxygen (metal–O) and hydroxyl oxygen, confirming strong metal–oxygen interactions and surface hydroxylation. The Fe 2p spectrum reveals Fe $2p_{3/2}$ and Fe $2p_{1/2}$ peaks with satellite features, confirming Fe^{3+} species, while Co 2p spectra indicate Co^{2+} oxidation states. The Zn 2p region confirms Zn^{2+} species, and Ca 2p peaks verify Ca^{2+} incorporation through coordination with carboxylate groups. These results confirm the formation of a stable Zn-Co-Fe/Ca biopolymer nanocomposite with metals present in oxidised states, resulting in surface reactivity and adsorption performance.

3.1.4 BET Surface Area Analysis

The N_2 adsorption–desorption isotherm of the nanocomposite, as shown in Fig. 5, exhibits a type IV isotherm with a pronounced hysteresis loop, characteristic of mesoporous materials. At low relative pressures (p/p_0 <0.3), adsorption increases gradually due to the formation of a single adsorbate layer on the surface. At higher relative pressures (p/p_0 >0.7), a sharp rise in adsorption volume corresponds to capillary condensation within mesopores. The close overlap between the adsorption and desorption

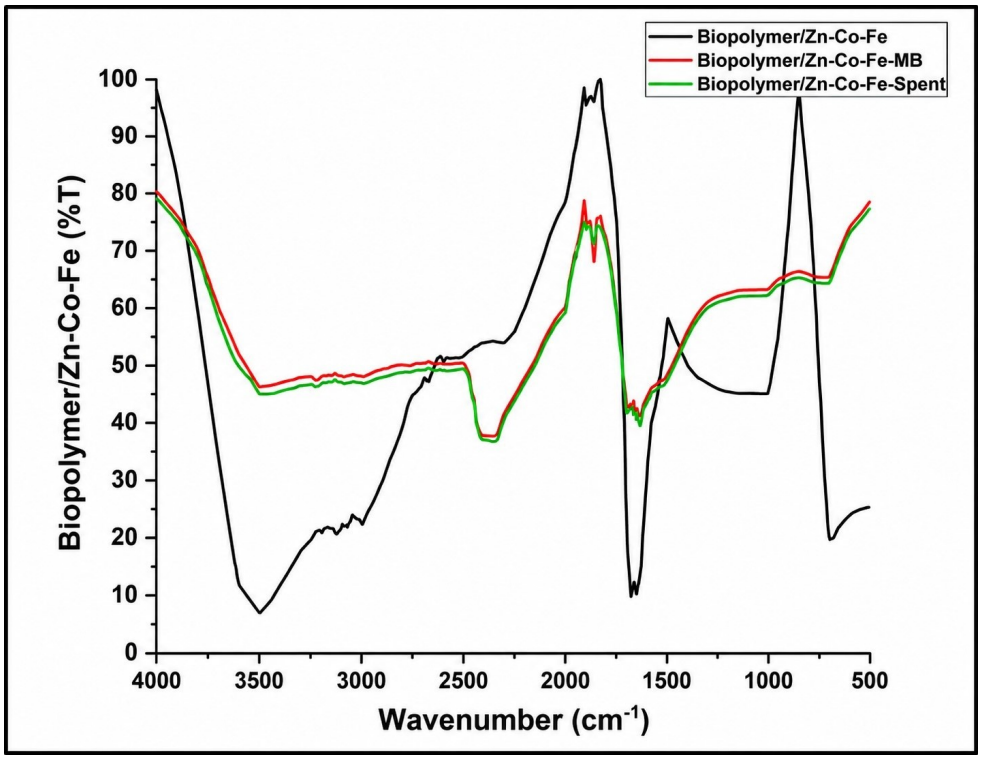

Fig. 2. FTIR spectra for the BPMNC bead. FTIR, Fourier transform infrared.

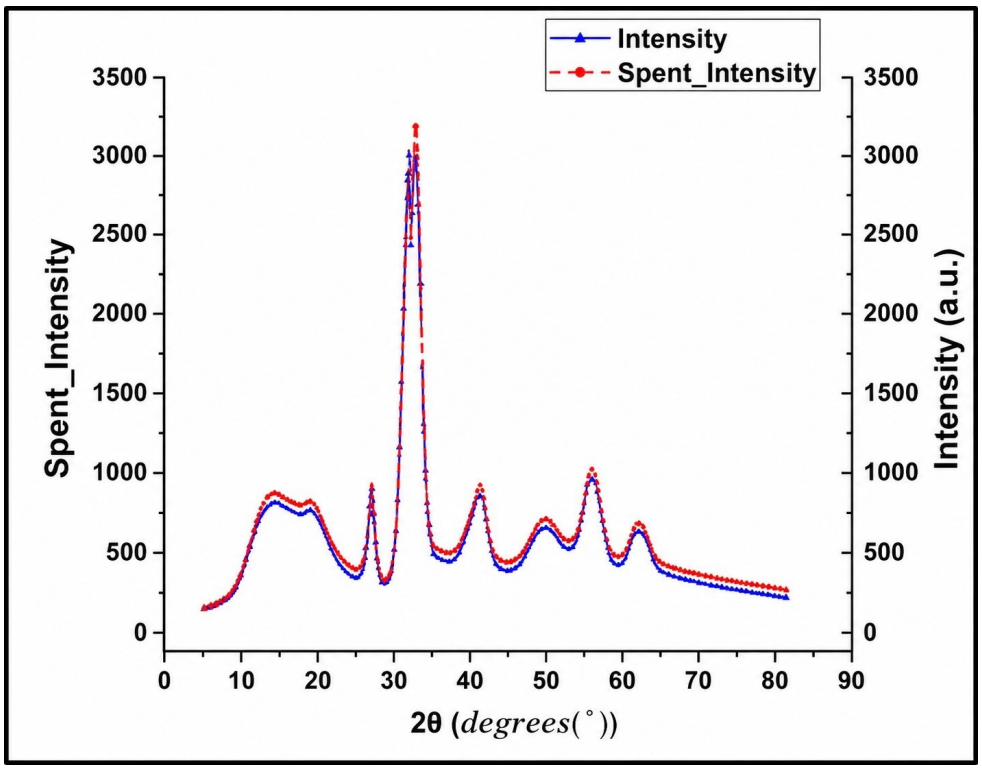

Fig. 3. XRD plot for the proposed adsorbent material. XRD, X-ray diffraction.

branches at low and intermediate pressures suggests a uniform pore structure and good structural stability of the nanocomposite. The pronounced hysteresis loop at higher p/p_0 values indicates the existence of interconnected mesopores, which are favourable for mass transfer and adsorption processes. The high volume of nitrogen adsorbed near $p/p_0 \approx 1.0$ reflects a well-developed porous network with accessible internal surfaces, attributed to the

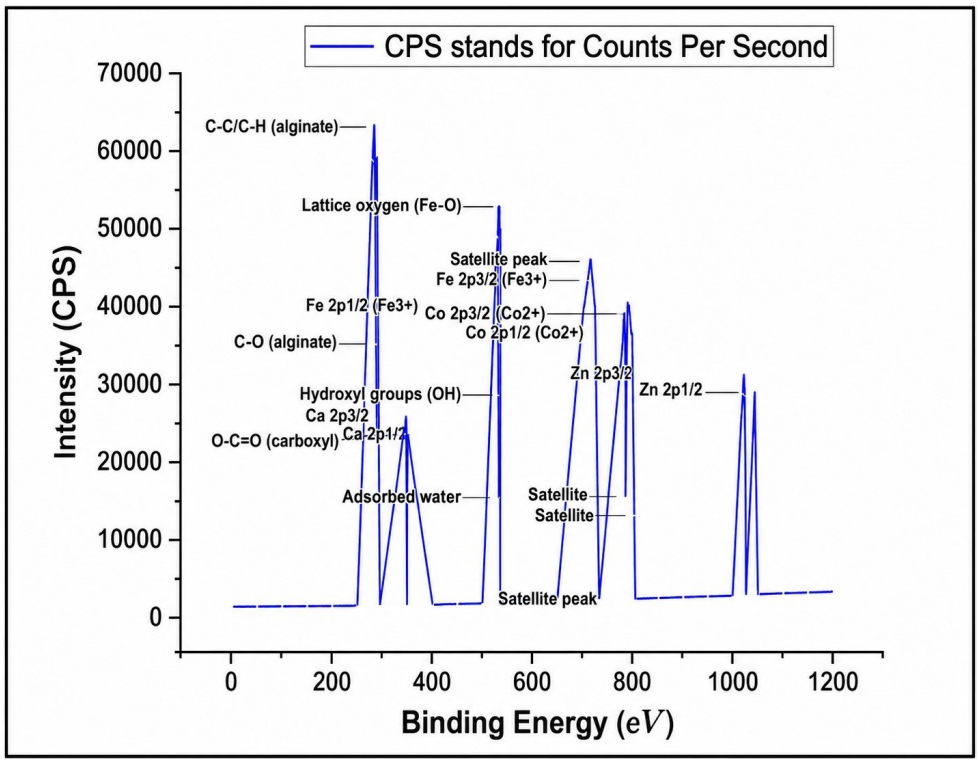

Fig. 4. XPS plot of BPMNC. XPS, X-ray photoelectron spectroscopy.

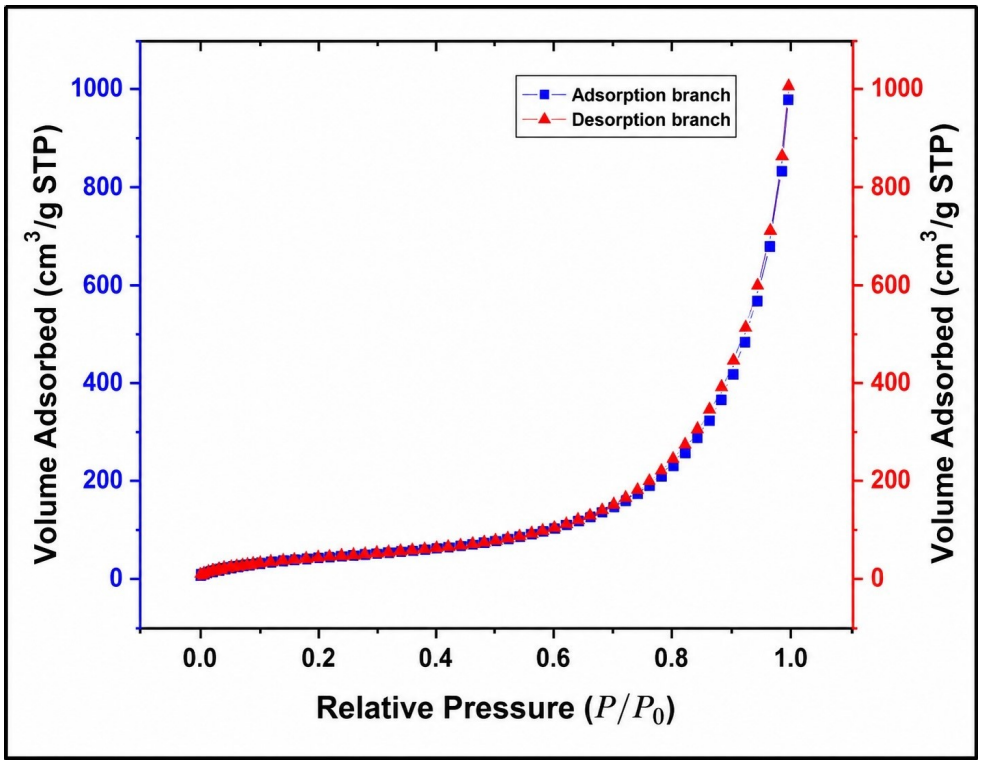

Fig. 5. BET plot of the proposed adsorbent. BET, Brunauer–Emmett–Teller.

homogeneous dispersion of Zn, Co, Fe, and Ca species within the biopolymer matrix. The incorporation of multi-metal components appears to prevent pore collapse and promote the formation of a stable porous architecture. The predominantly mesoporous structure facilitates efficient mass transfer and enhances adsorption efficiency toward dye molecules.

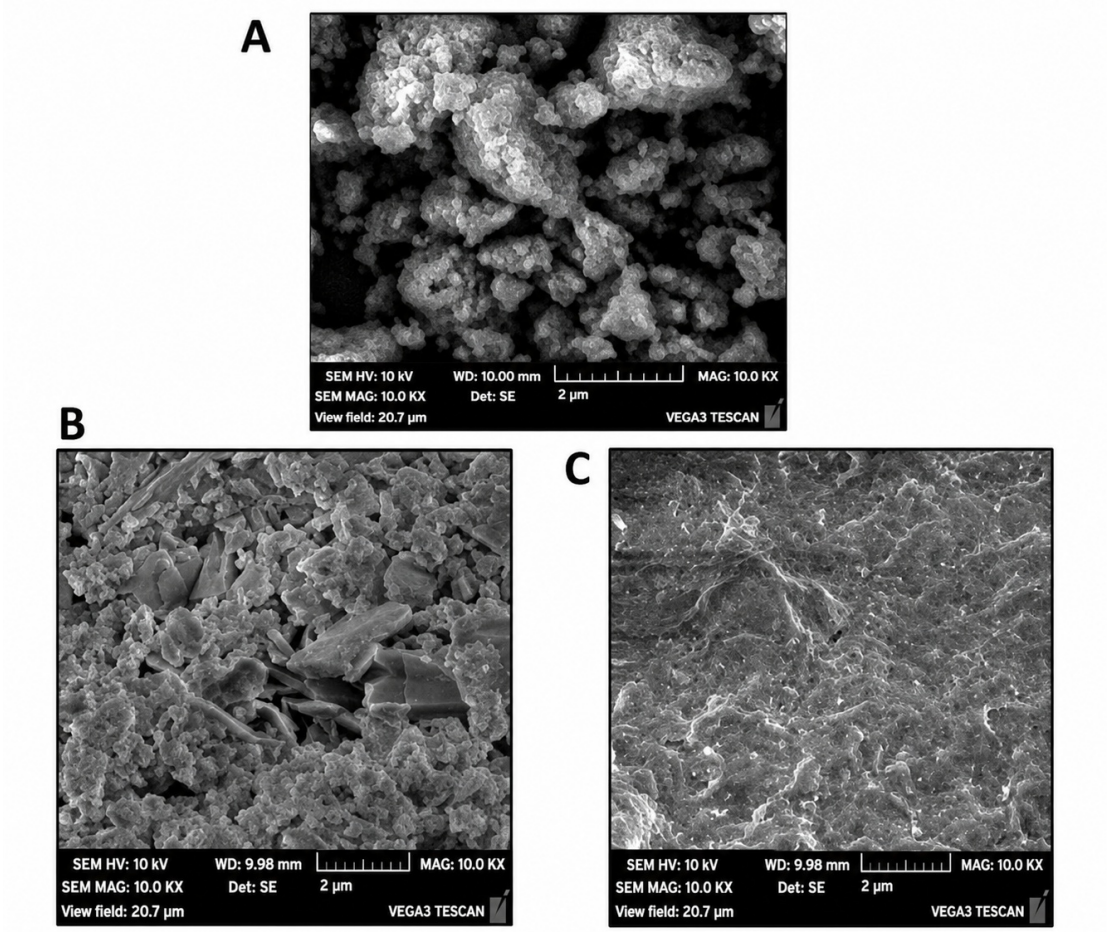

Fig. 6. SEM analysis. (A) Micrograph of Zn-Co-Fe Ferrite. (B) Micrograph of Alginate/Zn-Co-Fe/Ca Nanocomposite. (C) Micrograph of Alginate/Zn-Co-Fe/Ca/MB Nanocomposite. SEM, scanning electron microscopy; MB, methylene blue. Scale bar = 2 µm.

3.1.5 SEM Analysis

SEM imaging was employed to examine the surface morphology of Zn-Co-Fe ferrite and the biopolymer nanocomposite. Fig. 6A shows that the Zn-Co-Fe ferrite surface is porous and layered. Fig. 6B,C present the BPMNC composite bead surface before and after MB adsorption. In the pre-adsorption state, the beads exhibit a bright and porous structure with visible Zn-Co-Fe magnetic material on the surface. Following adsorption, the surface appears darker and less porous, indicating successful dye attachment. These morphological changes validate the effectiveness of the sorption process.

3.1.6 pH_pzc Analysis

Solution pH significantly influences adsorption efficiency by regulating surface charge interactions, as shown in Fig. 7. The maximum MB removal observed at pH 6 may be attributed to near-neutral surface conditions approaching the point of zero charge ($pH_pzc \approx 7.0$), where reduced electrostatic repulsion and favorable interaction dynamics enhance adsorption. At low pH, adsorption is suppressed due to proton competition for active sites. Above the pH_pzc, surface deprotonation induces a net negative charge, which theoretically favors electrostatic attraction with cationic MB molecules; however, excessive alkalinity may introduce charge-screening effects or structural alterations that limit further enhancement. The pH_pzc analysis confirms that the nanocomposite surface undergoes charge transition at approximately pH 7.0, where ΔpH equals zero. Below this value, positive ΔpH indicates a net positively charged surface, whereas above it, negative ΔpH reflects surface deprotonation and the development of negative charge. This surface charge transition rationalizes the observed optimum MB removal under near-neutral pH conditions.

3.1.7 TGA Analysis

The TG and derivative thermogravimetric (DTG) profiles, as shown in Fig. 8, reveal a multistage thermal decomposition pattern characterised by distinct mass-loss events and corresponding DTG maxima. An initial minor weight reduction below 150 °C is attributable to the release of physically adsorbed moisture and volatile constituents, followed

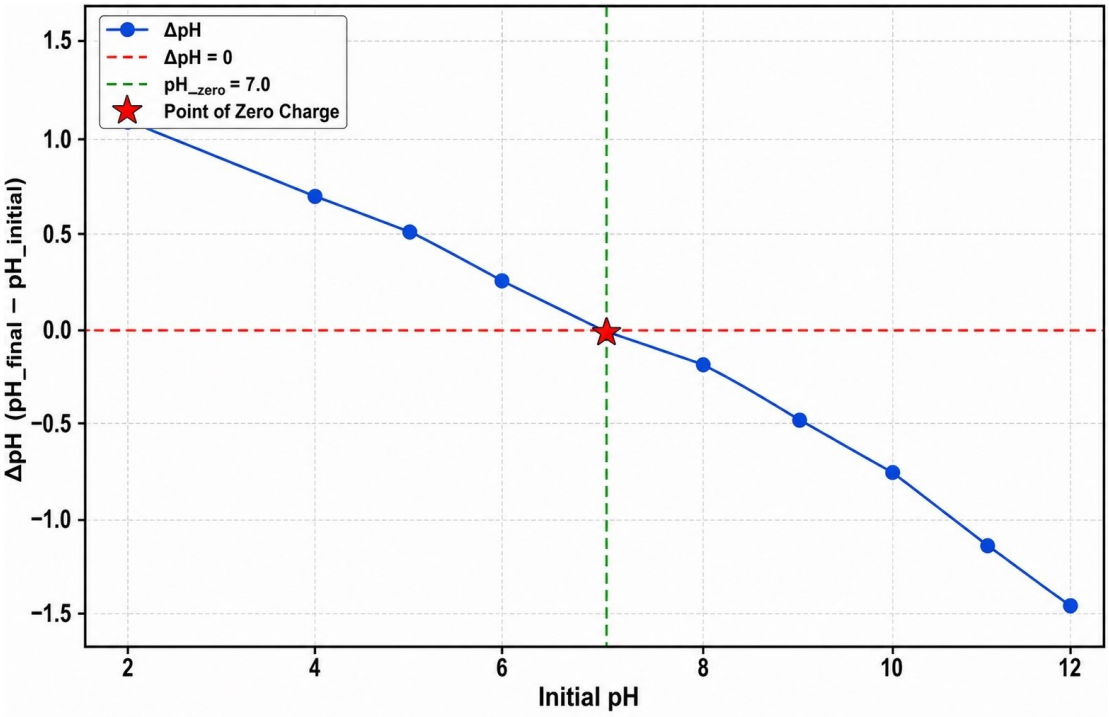

Fig. 7. pH_pzc plot of the adsorbent material. pH_pzc, point of zero charge.

by a pronounced degradation stage between 250 and 450 °C associated with primary structural decomposition. A secondary decomposition phase extending to 650 °C indicates further breakdown of more thermally stable fractions, after which the curve approaches a plateau, suggesting formation of a residual char or inorganic residue. Thus, the sharp DTG peaks and staged TG declines indicate complex thermal behaviour involving sequential reactions rather than a single-step degradation process.

3.2 Adsorption Studies of MB on BPMNC

Adsorption studies on magnetic composite beads, as shown in Figs. 9,10,11,12, focus on evaluating their ability to remove pollutants from aqueous solutions, thereby demonstrating their suitability for environmental remediation applications. The process typically begins with bead preparation, followed by exposure to contaminant-laden solutions under controlled conditions. Adsorption performance was assessed by systematically varying key operational parameters, such as initial dye concentration, contact time, solution pH, temperature, and adsorbent dosage, to determine the optimal conditions. Dye concentrations before and after adsorption were quantified using UV–visible spectrophotometry, as shown in **Supplementary Fig. 1A–E** provided in the **Supplementary Material** section, to calculate adsorption capacity and removal efficiency. Isotherm analysis using the Langmuir and the Freundlich models was employed to interpret the adsorption behaviour. In contrast, pseudo-first-order and pseudo-second-order kinetic models were used to elucidate adsorption kinetics and mechanisms. The magnetic nature of the beads enables easy separation from treated solutions using an external magnetic field, enhancing their practical applicability. Thus, adsorption studies provide valuable insights into the efficiency, capacity, and mechanisms of magnetic nanocomposite beads, supporting their design for diverse purification applications.

3.2.1 Effect of pH

pH plays a crucial role in sorption processes, as it influences both the ionisation state of the sorbate and the availability of active sites on the sorbent surface. Therefore, identifying the optimum pH is essential for effective adsorption. In this study, the influence of pH on MB adsorption was evaluated using 1 g of BPMNC beads in a 12 mg L^{-1} MB solution over a pH range of 3–10. Fig. 9 shows that adsorption efficiency increased markedly from 73% to 97% as the pH rose from 3 to 6, after which adsorption decreased significantly between pH 6 and 10. An adsorption efficiency of approximately 97% was attained at pH 6, demonstrating that this pH represents the optimum condition for MB removal by BPMNC beads.

3.2.2 Effect of Initial MB Concentration and Contact (Stirring) Time

Shaking time is an important parameter in adsorption studies, as insufficient agitation limits effective contact between the adsorbent and the dye solution. To evaluate this effect, MB concentrations of 4, 8, 12, 16, and 20 mg L^{-1} were investigated in 50 mL solutions while varying shak-

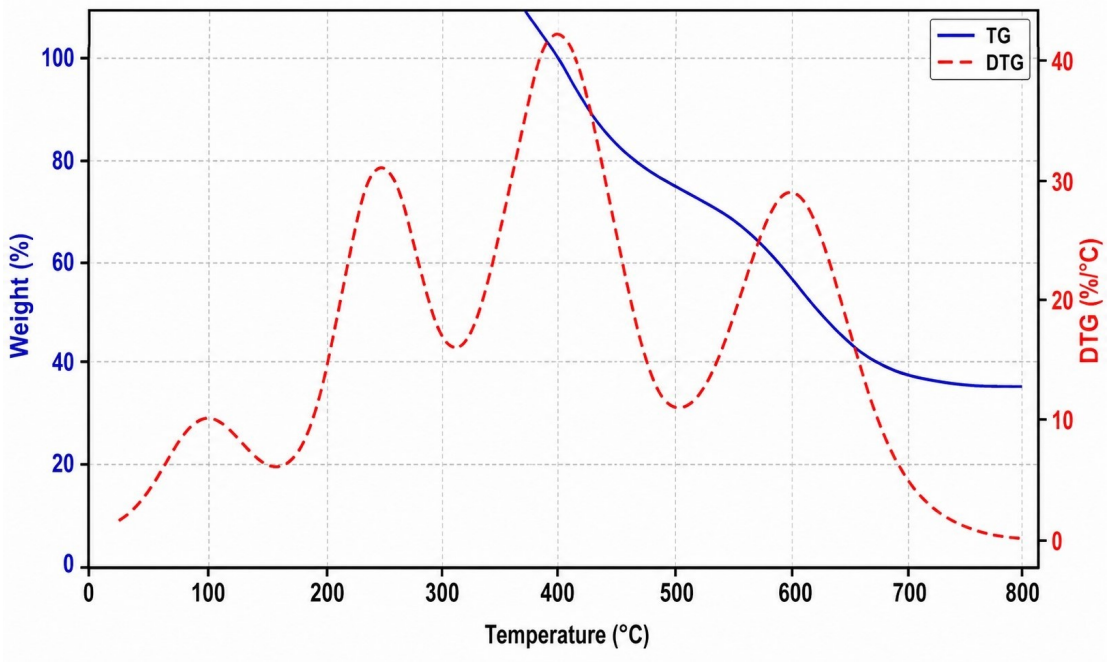

Fig. 8. TGA-DTG plot of BPMNC. TGA, thermogravimetric analysis; DTG, derivative thermogravimetric.

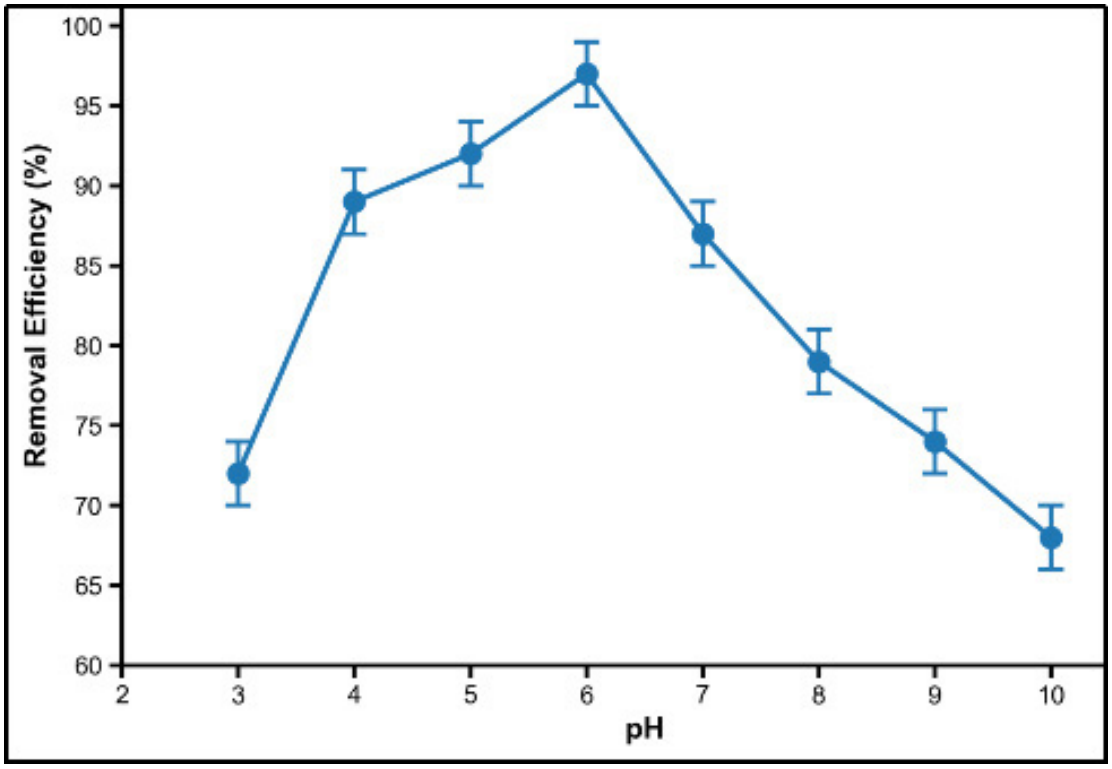

Fig. 9. Adsorption studies: Impact of pH on MB sorption onto BPMNC.

ing durations. The results shown in Fig. 10 demonstrate that MB adsorption onto BPMNC beads increased rapidly during the first 10–60 min, after which the adsorption rate slowed as equilibrium was approached. Only marginal improvements were observed at 70, 80, and 90 min, indicating that equilibrium had been reached. A shaking time of 60 min resulted in the highest adsorption efficiency among the tested durations. The adsorption percentage of MB was calculated using Eqn. 1:

$$Removal(\%) = \frac{C_i - C_f}{C_i} \times 100 \quad (1)$$

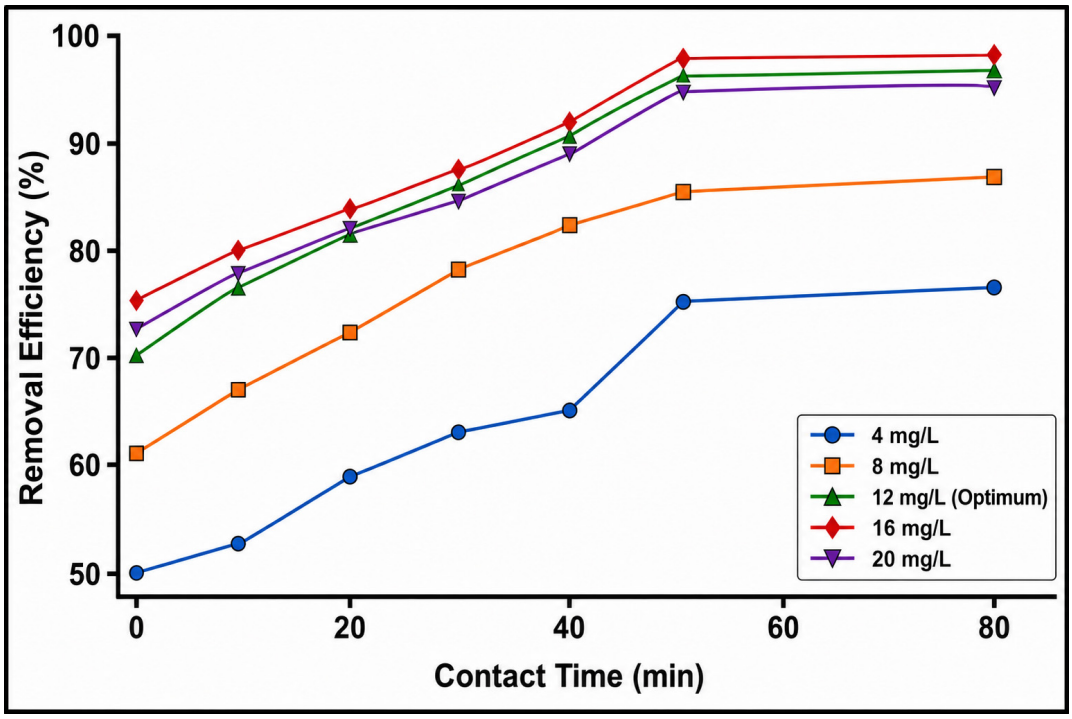

Fig. 10. Adsorption studies: Impact of MB concentration and shaking time on MB sorption onto BPMNC.

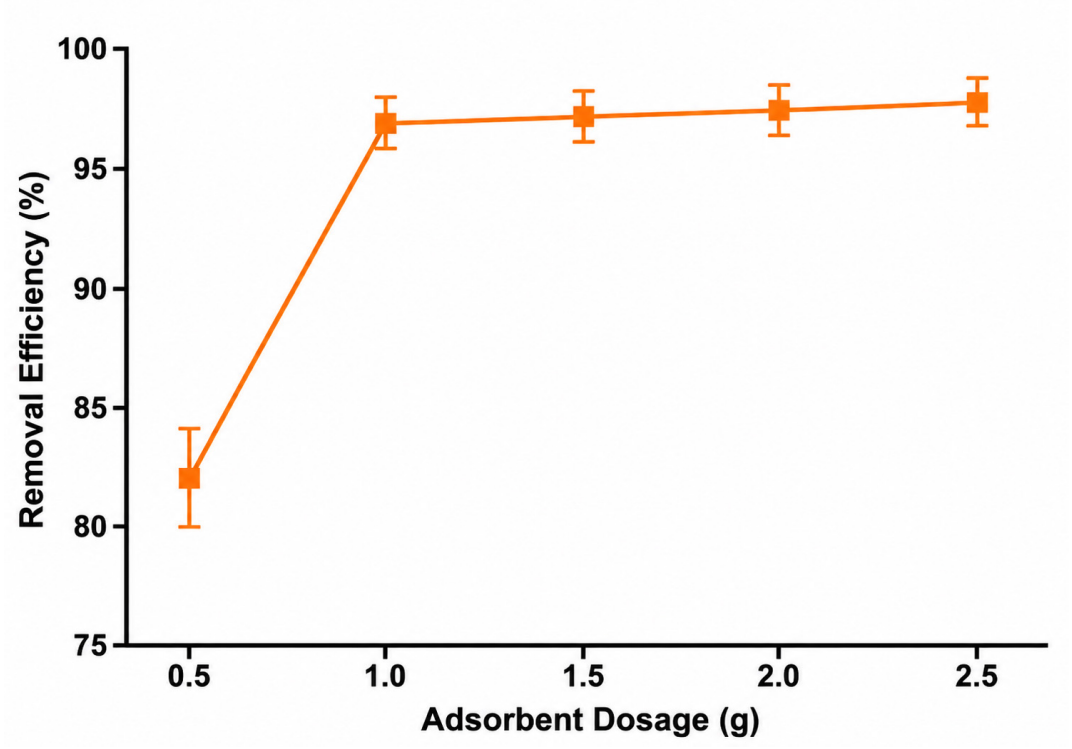

Fig. 11. Adsorption studies: Impact of dosage on MB sorption onto BPMNC.

where C_f and C_i represent the final and initial concentrations of MB after and before the adsorption process, respectively.

A maximum adsorption efficiency exceeding 97% was measured at an initial MB concentration of 12 mg L^{-1}; in contrast, efficiencies of 75%, 85%, 96%, and 96% were recorded at 4, 8, 16, and 20 mg L^{-1}, respectively. Accordingly, 12 mg L^{-1} was identified as the operationally optimal initial MB concentration for adsorption onto the BPMNC beads.

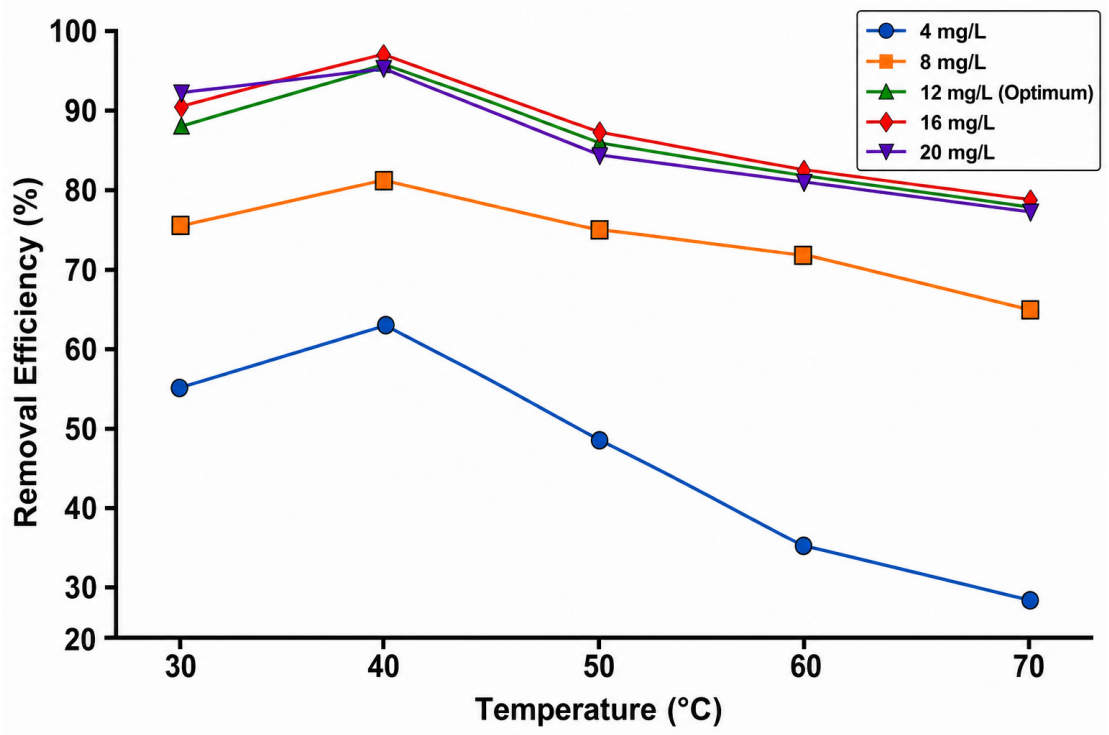

Fig. 12. Adsorption studies: Impact of temperature on MB sorption onto BPMNC.

3.2.3 Effect of BPMNC Dosage

The quantity of adsorbent plays a critical role in the adsorption process, making the selection of an appropriate amount of BPMNC beads essential for effective MB removal. In this study, 50 mL of a 12 mg L^{-1} MB solution was contacted with varying amounts of BPMNC beads (0.5–2.5 g) and agitated for 60 min. The results, shown in Fig. 11, indicate that even the lowest dose of 0.5 g achieved an adsorption efficiency of 82%. Increasing the dosage to 1.0 g improved the efficiency to 97%. Beyond 1.5 g, only marginal improvements in adsorption efficiency were observed due to equilibrium limitations, despite the availability of additional surface area at higher bead quantities. Consequently, increasing BPMNC dosage enhances adsorption until equilibrium conditions restrict further gains.

3.2.4 Temperature Effect on Adsorption

Temperature has a substantial impact on adsorption processes, especially the equilibrium capacity of the sorbent material. The effect of temperature on MB adsorption by BPMNC beads was examined over a range of 30–70 °C. Adsorption efficiency exceeded 97% at 40 °C, as presented in Fig. 12. At temperatures below 40 °C, the adsorption efficiency decreased due to reduced physical interactions between MB molecules and BPMNC nanoparticles. These findings indicate that 40 °C is the operationally optimal temperature for MB adsorption onto BPMNC beads.

3.2.5 Influence of Parallel/Coexisting Parameters

Fig. 9 through 12 summarise the effects of key operational parameters on the adsorption of MB onto BPMNC. As shown in Fig. 9, the percentage removal of MB increases with pH from acidic to near-neutral conditions, reaching a maximum around pH 6, and then decreases at higher pH values. This behaviour can be attributed to changes in surface charge and the ionisation of functional groups on BPMNC, where moderate pH conditions favour electrostatic attraction between positively charged MB molecules and negatively charged adsorption sites. In contrast, excessive alkalinity may reduce adsorption due to increased competition with hydroxyl ions. The combined effect of initial MB concentration and shaking time is presented in Fig. 10, where adsorption increases rapidly with contact time for all concentrations, particularly during the initial stages, and gradually approaches equilibrium. Higher initial MB concentrations result in increased adsorption due to a greater concentration gradient and enhanced mass transfer driving force. Fig. 11 demonstrates the effect of BPMNC dosage on MB removal, showing a sharp increase in removal efficiency with increasing adsorbent dose up to an optimum value, beyond which the removal percentage remains nearly constant. This trend is associated with the increased availability of active adsorption sites at higher dosages, followed by site saturation and aggregation effects at higher dosages. As shown in Fig. 12, MB removal efficiency increases with temperature up to an optimum value and then gradually decreases at higher tem-

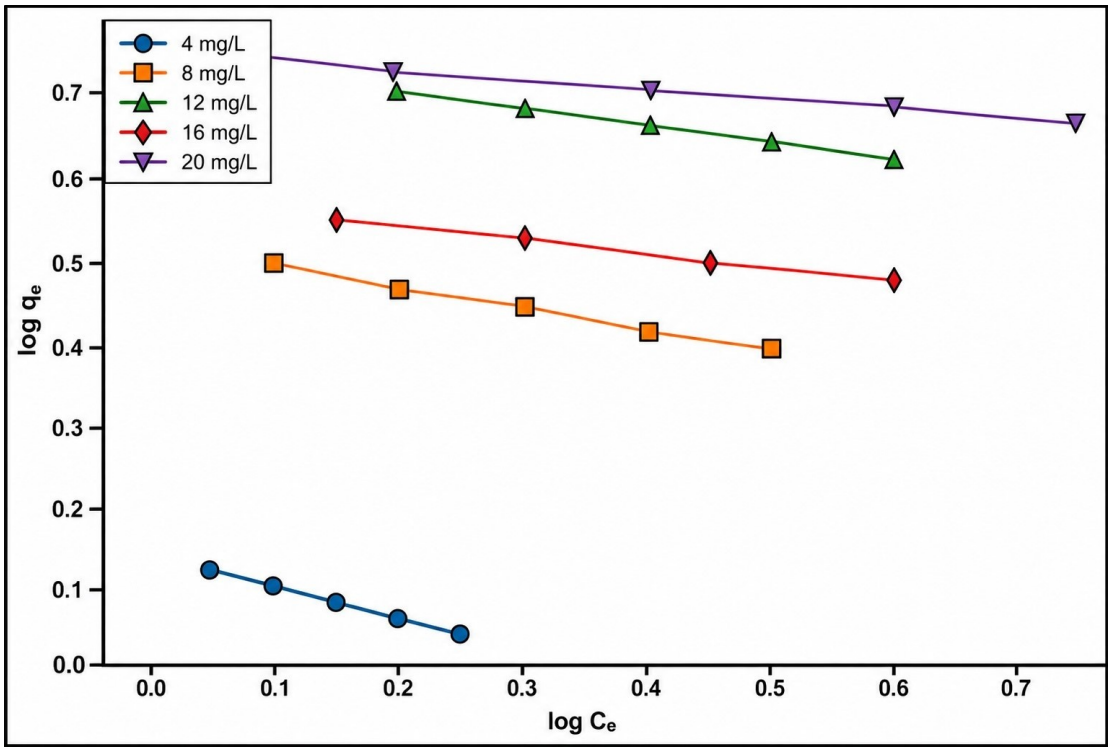

Fig. 13. Adsorption study: Freundlich isotherm study of MB sorption on BPMNC.

peratures, indicating the exothermic nature of the adsorption process. Taken together, the results indicate that MB adsorption onto BPMNC is strongly influenced by solution pH, adsorbent dosage, initial dye concentration, contact time, and temperature, collectively determining adsorption efficiency and stability.

3.3 Adsorption Modelling and Mechanistic Evaluation

Figs. 13,14,15 show the adsorption behaviour of MB onto BPMNC through isotherm modelling, kinetic evaluation, and thermodynamic assessment. The Freundlich isotherm plot shown in Fig. 13 exhibited a linear relationship between log qe and log Ce, indicating multilayer adsorption on a heterogeneous surface. The slope values (1/n) were found to be less than unity (0.115–0.353), confirming favorable adsorption of methylene blue onto BPMNC. The corresponding n values (2.83–8.69) further support the favorable adsorption process. The relatively high correlation coefficients (R^2 = 0.85–0.96) indicate that the Freundlich model adequately describes the adsorption behavior Fig. 13.

Fig. 14 presents the pseudo-first-order kinetic plots for MB adsorption onto BPMNC at different initial dye concentrations. Although a generally increasing trend of log(qe − qt) with contact time is observed, the linearity of the plots is only moderate, as reflected by the relatively low correlation coefficients (R^2 = 0.7236–0.7901) listed in Table 2. These results indicate that the pseudo-first-order model does not adequately describe the adsorption kinetics over the entire adsorption period. Comparison with the pseudo-second-order model reveals substantially higher correlation coefficients (R^2 = 0.9614–0.9808), suggesting that the adsorption process is better represented by the pseudo-second-order kinetic model. Therefore, the pseudo-first-order model may describe only the initial stage of adsorption, whereas the overall adsorption behaviour is governed by pseudo-second-order kinetics ig. 14. The Van't Hoff plot, as shown in Fig. 15, exhibits a strong linear relationship between ln K and 1/T, as evidenced by the excellent regression fit (R^2 = 0.99), indicating that the thermodynamic behaviour of the system conforms closely to classical equilibrium theory. The negative slope (–3436.1) signifies an exothermic process, reflecting a decrease in equilibrium constant with increasing temperature. The small, consistent error bars suggest high experimental precision and reproducibility across the studied temperature range. Thus, the linearity and statistical robustness of the fit confirm the reliability of the derived thermodynamic parameters and support the assumption of temperature-independent enthalpy within the investigated interval. Thus, the Freundlich isotherm, kinetic, and thermodynamic analyses collectively confirm that MB adsorption onto BPMNC is a heterogeneous, kinetically favourable, and endothermic process, highlighting the strong potential of BPMNC as an efficient and thermally stable adsorbent for dye removal applications.

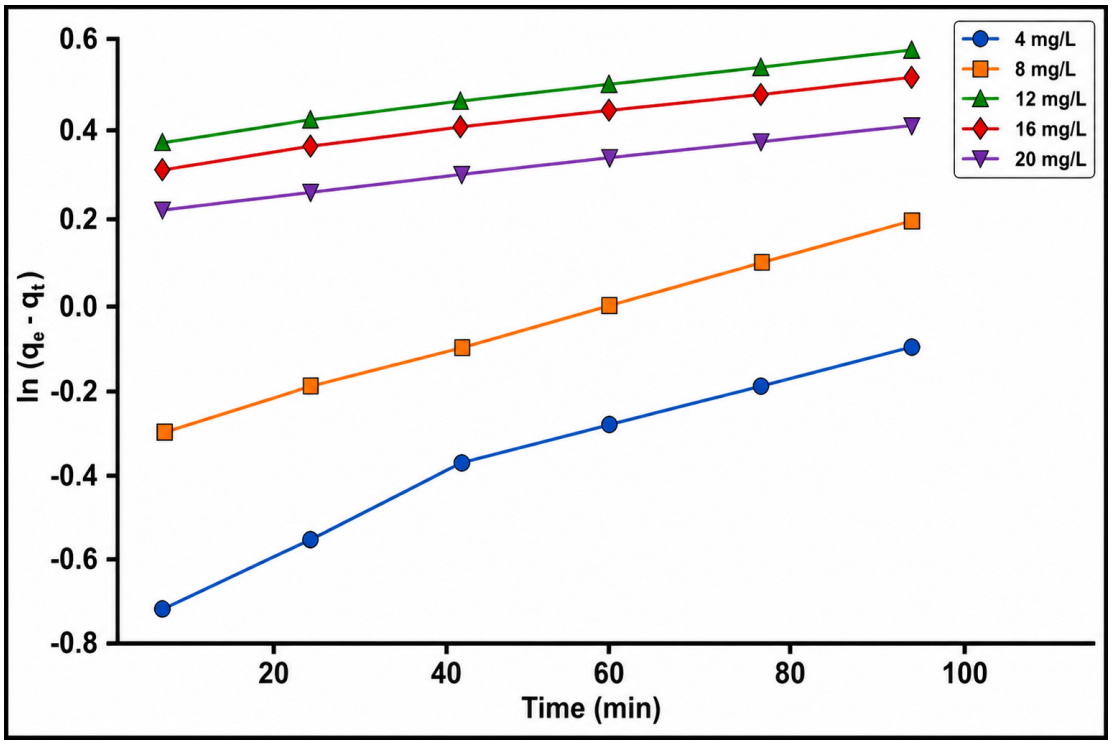

Fig. 14. Adsorption study: Plot of pseudo-first order kinetics for MB sorption on BPMNC.

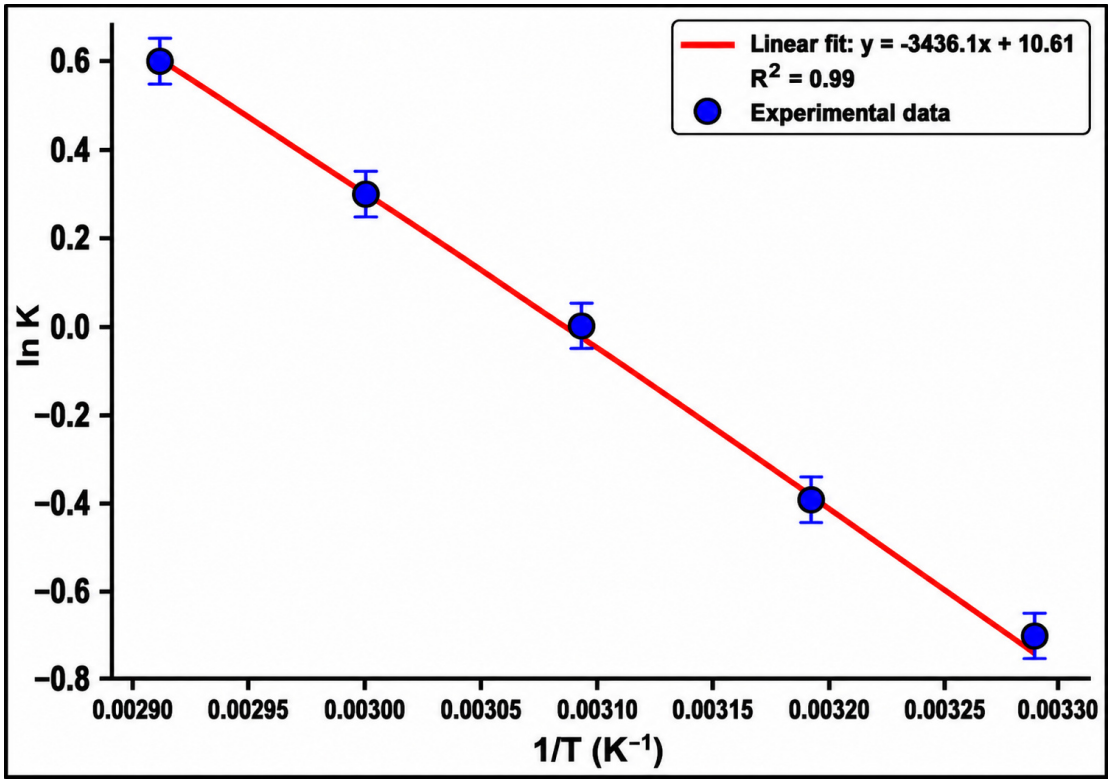

Fig. 15. Adsorption study: Van't Hoff plot for MB sorption on BPMNC.

3.3.1 Isotherm Studies

Commonly used adsorption isotherm models, including the Langmuir and the Freundlich models, were applied in the present study to interpret the experimental data. The Freundlich model assumes adsorption on a heterogeneous surface with sites of varying adsorption energies.

The Freundlich isotherm is expressed in the following forms Eqns. 2,3:

Table 1. Isotherm variables for the adsorption of MB.

Isotherm models	Variables	C_0 (mg L^{-1})				
		4	8	12	16	20
Langmuir model- 1	q_m (mg g^{-1})	0.7801	2.1640	4.1728	2.7860	3.7012
	K_a (L mg^{-1})	1.9683	2.1066	5.3490	3.7406	4.0143
	R^2	0.9803	0.9890	0.9892	0.9911	0.9941
Langmuir model- 2	q_m (mg g^{-1})	1.8502	2.2774	4.6188	3.0202	3.9241
	K_a (L mg^{-1})	2.3797	2.4652	13.2160	7.3501	7.0051
	R^2	0.8931	0.8477	0.5492	0.6387	0.7005
Langmuir model- 3	q_m (mg g^{-1})	2.0921	6.0688	22.1057	17.1572	22.1708
	K_a (L mg^{-1})	0.4083	0.3787	0.1912	0.1706	0.1731
	R^2	0.8865	0.8394	0.7830	0.7206	0.7633
Langmuir model- 4	q_m (mg g^{-1})	2.9332	7.4082	23.3197	23.2411	28.3883
	K_a (L mg^{-1})	0.3150	0.3244	0.1850	0.1300	0.1388
	R^2	0.7950	0.8305	0.8301	0.7206	0.7633
Freundlich model	n	2.8321	3.1698	7.5461	8.2787	8.6918
	K_F (mg g^{-1}) (L $g^{-1})^{1/n}$	1.7131	0.5791	0.3280	0.5724	0.3961
	R^2	0.9654	0.9588	0.8501	0.8854	0.9077

MB, methylene blue.

Freundlich non-linear form:

$$q_e = K_F C_e^{1/n} \quad (2)$$

Freundlich linearised form:

$$log q_e = log\,(K_F) + \frac{1}{n} log\,(C_e) \quad (3)$$

where

q_e (mg g^{-1}) is the equilibrium adsorption capacity of MB,

C_e (mg L^{-1}) is the equilibrium concentration of MB in solution,

K_F is the Freundlich constant related to adsorption capacity ((mg g^{-1})(L $mg^{-1})^{1/n}$), and

1/n represents the adsorption intensity.

MB adsorption in the present study is significant, with *n* values ranging from 2 to 8. The adsorption behaviour was further analysed using the Langmuir isotherm model, which assumes monolayer adsorption on a homogeneous surface with identical adsorption sites and no lateral interaction between adsorbed molecules at the BPMNC bead interface. The absence of surface expansion on BPMNC nanoparticles suggests that the adsorption process follows a single-layer mechanism. The various forms of the Langmuir and the Freundlich models are summarised in Table 1.

The Langmuir isotherm is expressed as Eqns. 4,5:

Langmuir non-linear form:

$$q_e = \frac{q_m K_a C_e}{1 + K_a C_e} \quad (4)$$

Langmuir linearised form:

$$\frac{C_e}{q_e} = \frac{1}{q_m} C_e + \frac{1}{K_a q_m} \quad (5)$$

where

q_e (mg g^{-1}) is the equilibrium adsorption capacity,

C_e (mg L^{-1}) is the equilibrium concentration of MB in solution,

q_m (mg g^{-1}) represents the maximum monolayer adsorption capacity of MB per unit mass of BPMNC, and

K_a (L mg^{-1}) is the Langmuir constant related to the affinity between adsorption sites and MB molecules.

Figs. 16,17,18,19 present the Langmuir isotherm analysis for MB adsorption onto BPMNC beads using different linear and non-linear model representations. As shown in Fig. 16, the relationship between equilibrium adsorption capacity and equilibrium concentration exhibits a typical Langmuir-type behaviour, indicating progressive occupation of homogeneous adsorption sites on the BPMNC surface with increasing MB concentration. The linearised Langmuir plot in Fig. 17 ($1/q_e$ versus $1/C_e$) shows good linearity for all studied concentrations (4–20 mg L^{-1}), confirming the applicability of the Langmuir model and suggesting monolayer adsorption on a finite number of identical active sites. Fig. 18 further supports this observation, where the Langmuir model parameters derived from alternative linearisation forms display consistent trends, indicating uniform adsorption energies and negligible lateral interactions between adsorbed MB molecules. Additionally, the plots in Fig. 19 demonstrate a strong correlation between experimental and model-predicted adsorption capacities, particularly at higher concentrations, re-

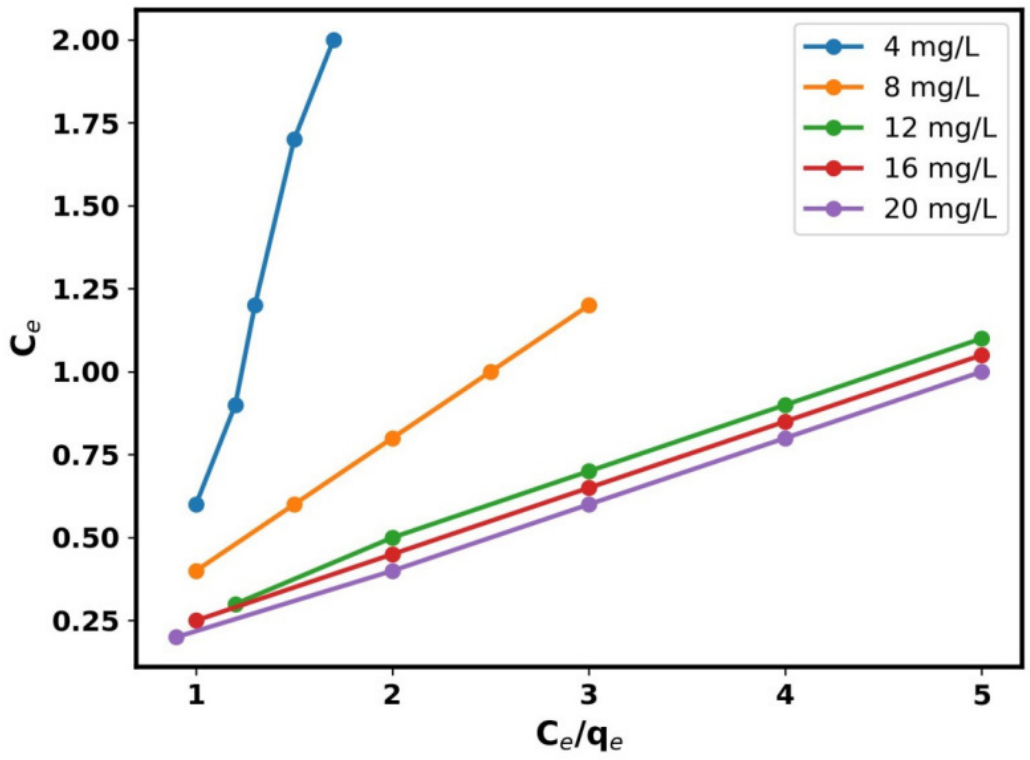

Fig. 16. Langmuir isotherm analysis: Langmuir isotherm study of MB adsorption on BPMNC.

flecting the saturation of available adsorption sites. Taken together, Langmuir model conformity suggests monolayer MB adsorption on a homogeneous BPMNC surface, consistent with chemisorption-dominated kinetics.

3.3.2 Kinetic Studies

To interpret the experimental data, Lagergren's pseudo-first-order and pseudo-second-order kinetic models were applied. According to the pseudo-first-order model, the adsorption rate of MB is proportional to the difference between the equilibrium adsorption capacity and the amount adsorbed at any given time. Lagergren (1898) [37] reported a significant relationship between the rate of adsorption onto a solid surface and the concentration difference driving the adsorption process. The kinetic variables for the adsorption of MB are described in Table 2.

The pseudo-first-order kinetic model is expressed as Eqn. 6:

$$log\,(q_e - q_t) = log\,(q_e) - \frac{K_1 t}{2.303} \tag{6}$$

where

q_e (mg g^{-1}) is the equilibrium adsorption capacity of MB on BPMNC beads,

q_t (mg g^{-1}) is the amount of MB adsorbed at time t, and

K_1 (min^{-1}) is the pseudo-first-order rate constant.

The pseudo-second-order kinetic model, which assumes that the rate-limiting step involves chemisorption through electron sharing or exchange between adsorbent and adsorbate, was also employed to analyse the experimental results. The pseudo-second-order kinetic equation is given as Eqn. 7:

$$\frac{t}{q_t} = \frac{1}{K_2 q_e^2} + \frac{1}{q_e} t \tag{7}$$

where

q_e (mg g^{-1}) is the equilibrium adsorption capacity,

K_2 (g mg^{-1}·min) is the pseudo-second-order rate constant, and

q_t (mg g^{-1}) is the amount of MB adsorbed at time t.

The pseudo-second-order kinetic behaviour of MB adsorption onto BPMNC beads was evaluated using four different model representations, as shown in Figs. 20,21,22,23. As depicted in Fig. 20, the experimental adsorption capacity increased rapidly during the initial contact period for all initial MB concentrations (4–20 mg L^{-1}). It then gradually reached equilibrium with time, indicating a high affinity between MB molecules and the active sites of the BPMNC beads.

The increasing equilibrium uptake with higher initial concentrations reflects an enhanced mass transfer driving

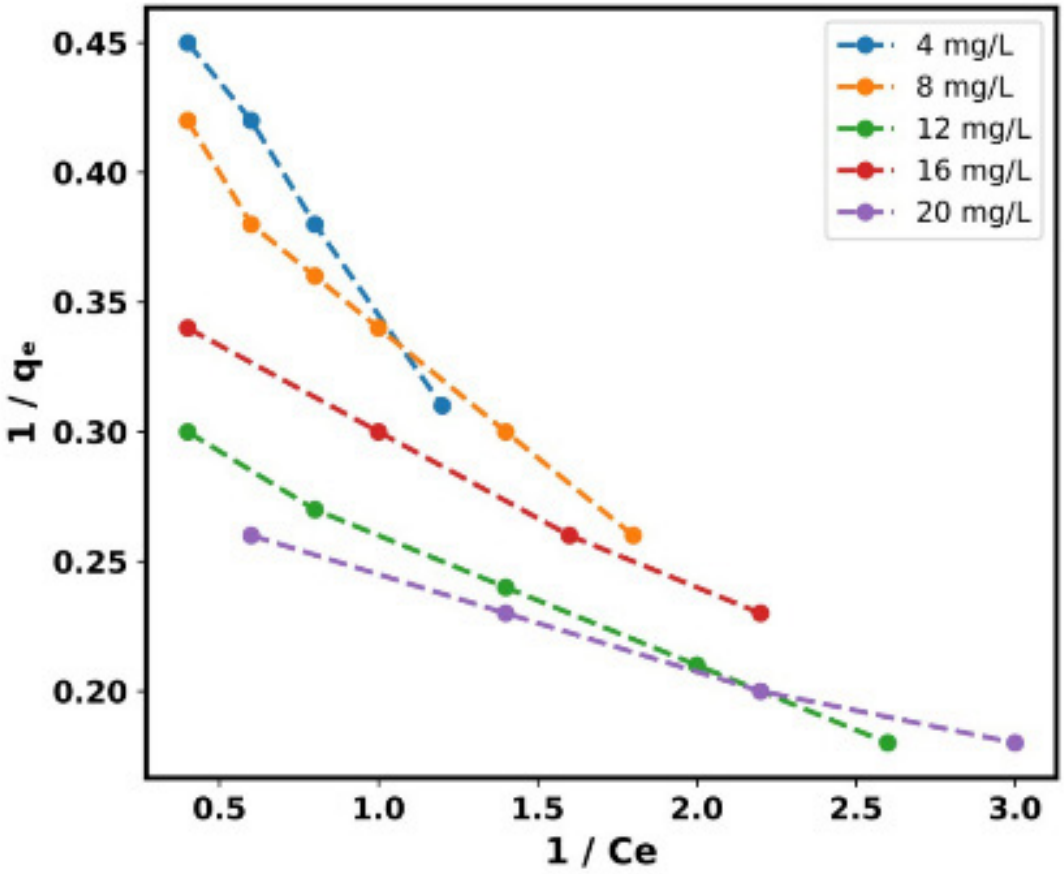

Fig. 17. Langmuir isotherm analysis: Langmuir isotherm analysis of MB adsorption on BPMNC beads.

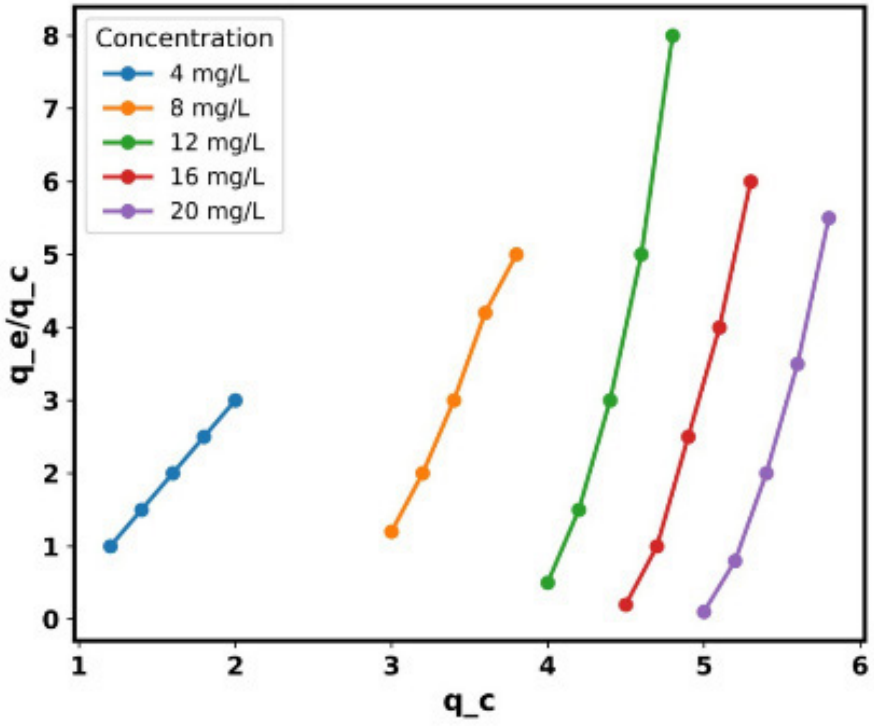

Fig. 18. Langmuir isotherm analysis: Langmuir isotherm model for MB adsorption on BPMNC beads.

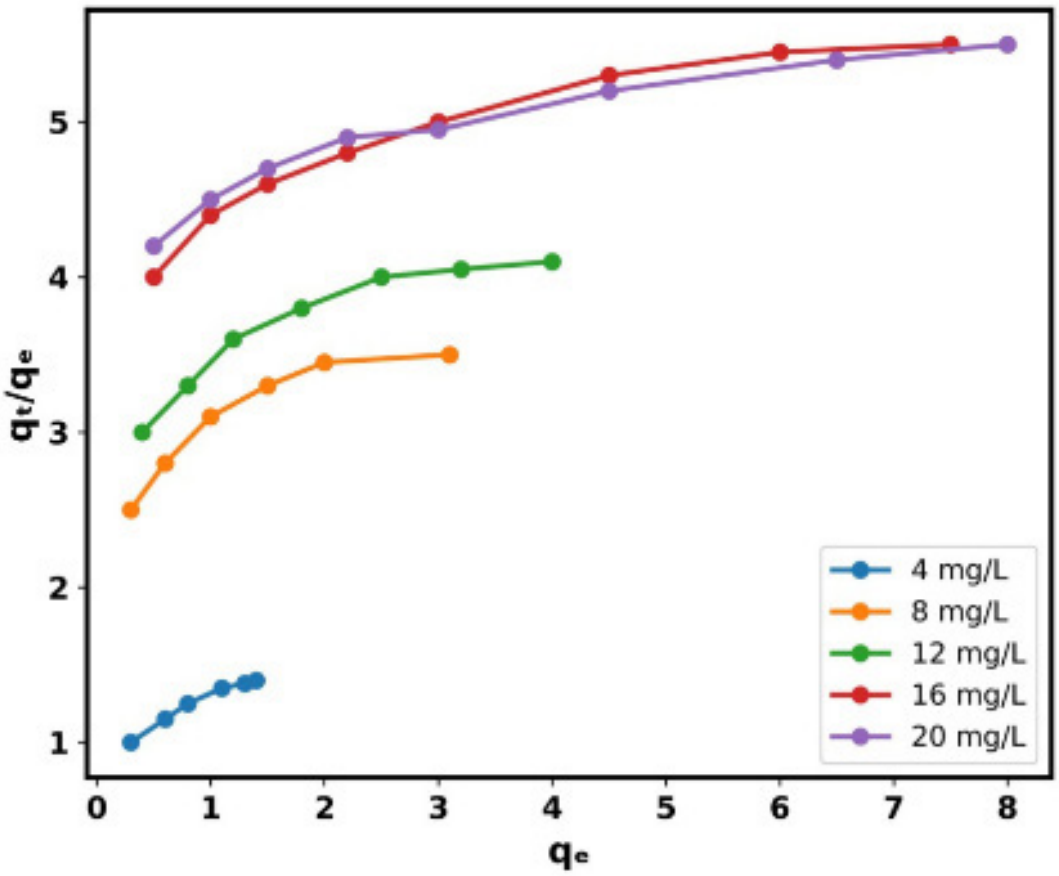

Fig. 19. Langmuir isotherm analysis: Langmuir isotherm analysis of MB adsorption on BPMNC beads.

Table 2. Kinetic variables for the adsorption of MB.

Kinetics models	Variables	C_0 (mg L^{-1})				
		4	8	12	16	20
Pseudo-first-order model	K_1 (g mg^{-1} min^{-1})	0.0341	0.0136	0.0105	0.0103	0.0078
	q_e (mg g^{-1})	0.5305	0.4303	0.3701	0.6102	0.3781
	R^2	0.7481	0.7236	0.7332	0.7784	0.7901
	q_e.exp (mg g^{-1})	0.8500	1.7500	2.8200	3.7400	4.6700
Pseudo-second-order model 1	K_2 (g mg^{-1} min^{-1})	0.1981	0.1593	0.1838	0.2491	0.3232
	q_e.cal (mg g^{-1})	0.4307	0.4937	0.3953	0.3208	0.2795
	R^2	0.9614	0.9708	0.9779	0.9773	0.9808
Pseudo-second–order model 2	K_2 (g mg^{-1} min^{-1})	0.3221	0.2231	0.2740	0.3209	0.2996
	q_e.cal (mg g^{-1})	0.5403	0.6147	0.3674	0.3741	0.4078
	R^2	0.4578	0.5774	0.5177	0.5722	0.5741
Pseudo-second-order model 3	K_2 (g mg^{-1} min^{-1})	1.9575	1.6364	3.0772	4.1271	3.6805
	q_e.cal (mg g^{-1})	0.0600	0.0700	0.0400	0.0300	0.0400
	R^2	0.6610	0.7867	0.7820	0.7441	0.7404
Pseudo-second–order model 4	K_2 (g mg^{-1} min^{-1})	45.8002	61.4695	188.5025	234.8640	202.7280
	q_e.cal (mg g^{-1})	2.9440	4.3202	3.6437	2.6911	2.9095
	R^2	0.6610	0.7867	0.7820	0.7441	0.7404

force. Fig. 21, representing the linearised pseudo-second-order Model 2 ($1/q_t$ vs. $1/t$), exhibits good linearity across all concentrations, suggesting that the adsorption rate is predominantly controlled by chemisorption involving valence forces through electron sharing or exchange between MB molecules and the functional groups on the bead surface.

Similarly, the plots in Fig. 22 (t/q_t vs. q_t, Model 3) and Fig. 23 (q_t vs. t/q_t, Model 4) also show consis-

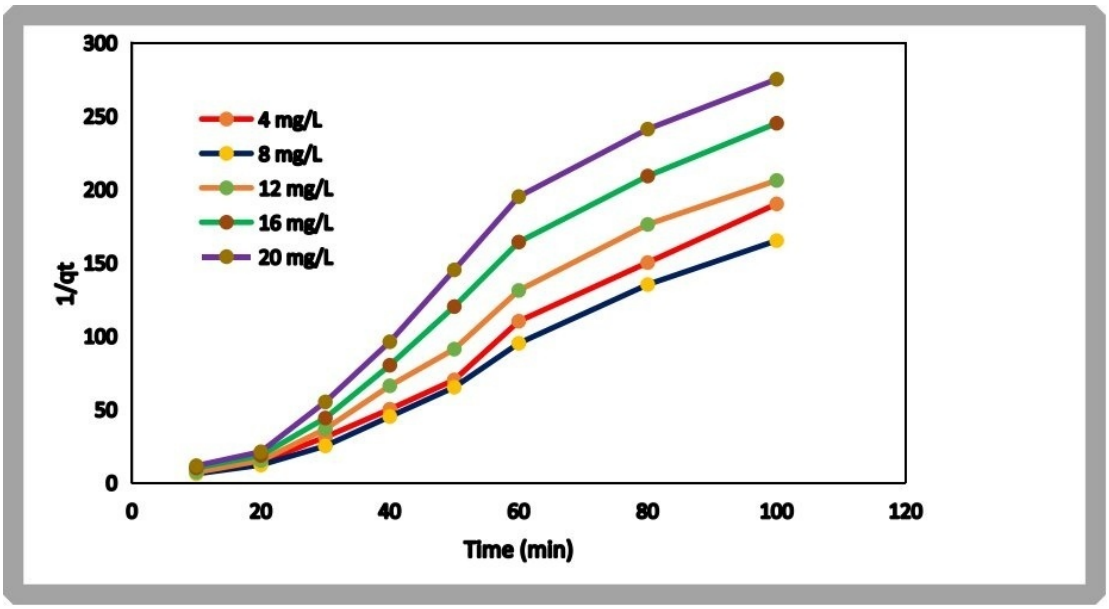

Fig. 20. Pseudo-second-order Kinetics Study: Pseudo-second-order Kinetics model 1 plot for MB Adsorption.

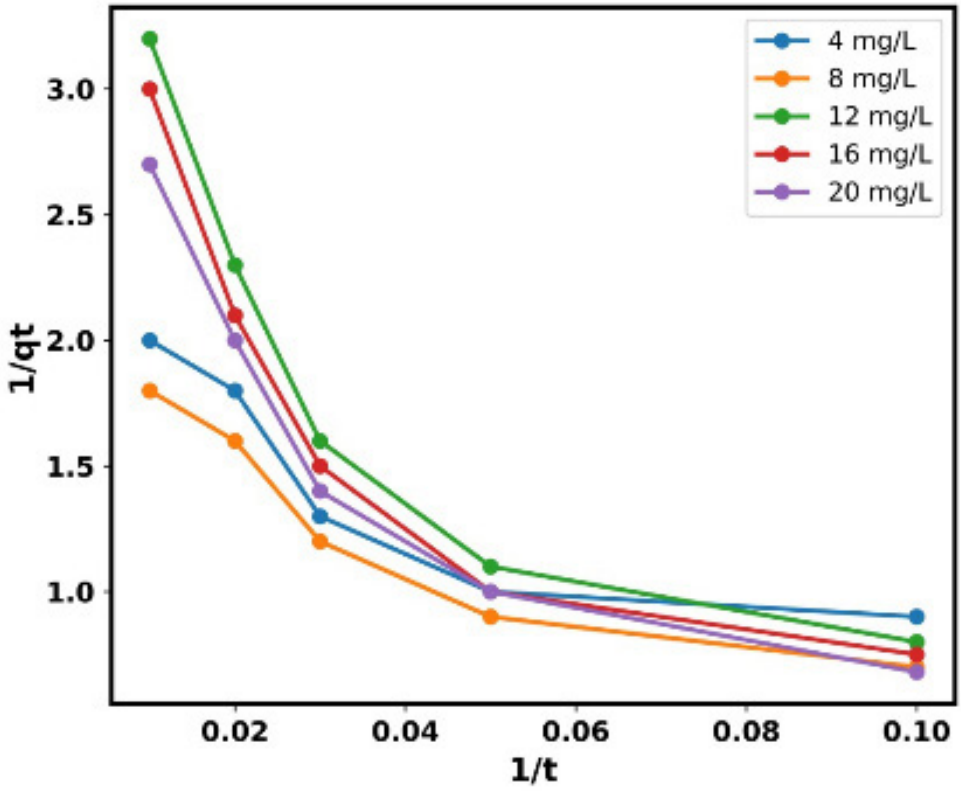

Fig. 21. Pseudo-second-order Kinetics Study: Pseudo-second-order model 2 plot on adsorption of MB onto BPMNC beads.

tent linear trends with high correlation, further confirming the applicability of the pseudo-second-order kinetic model. The close agreement between experimental and calculated adsorption capacities across all models indicates that the adsorption process is governed by surface reactions rather than solely by diffusion. In summary, the successful fitting of all pseudo-second-order models demonstrates that MB adsorption onto BPMNC beads is predominantly governed by chemisorption, supported by strong interactions between dye molecules and the BPMNC.

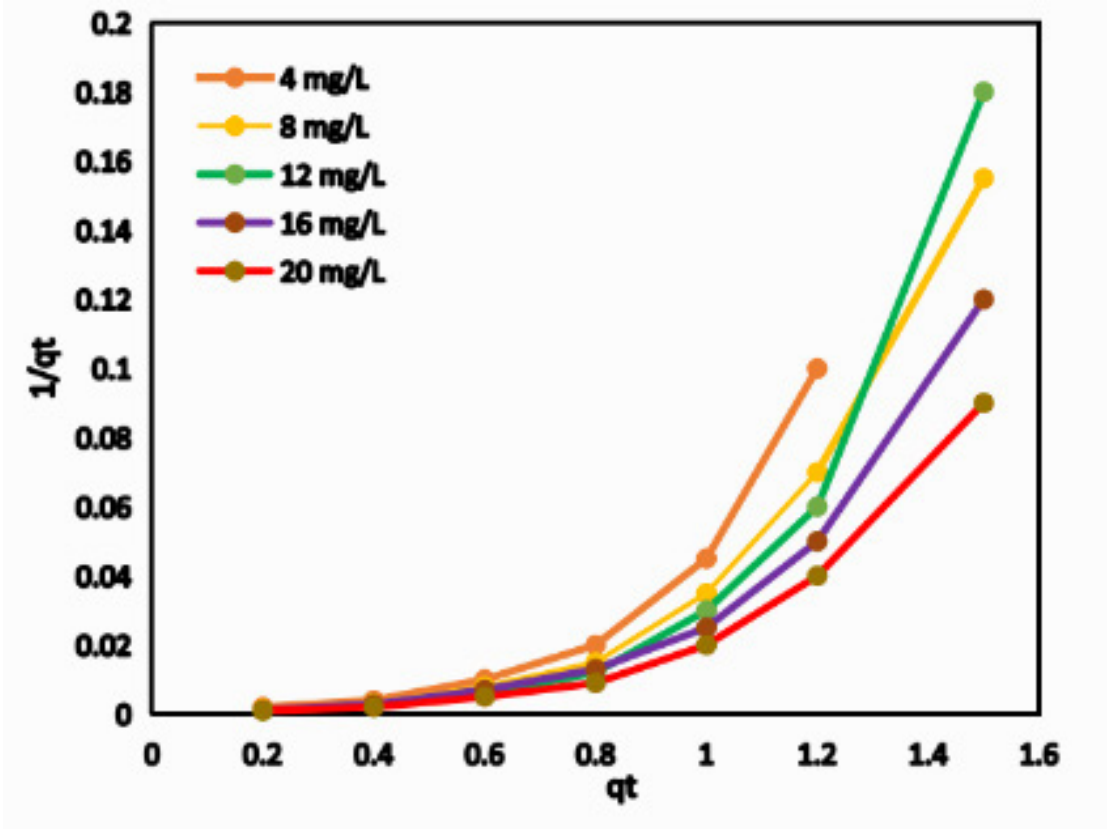

Fig. 22. Pseudo-second-order Kinetics Study: Pseudo-second-order model 3 plot on adsorption of MB.

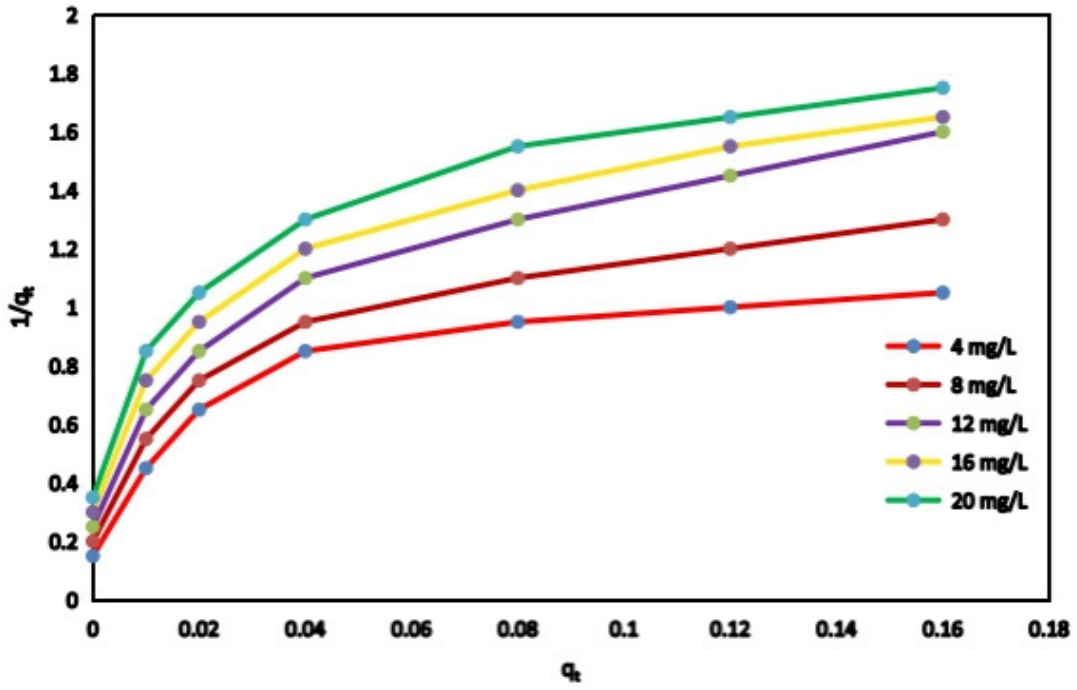

Fig. 23. Pseudo-second-order Kinetics Study: Pseudo-second-order model 4 plot on the adsorption of MB onto BPMNC beads.

3.3.3 Diffusion Mechanism

The intraparticle diffusion model is employed to examine the diffusion mechanism involved in the adsorption process. Adsorption and diffusion typically occur in three main stages: (i) mass transfer of the adsorbate through the boundary layer, corresponding to diffusion across the liquid

film surrounding the particles; (ii) adsorption of the adsorbate onto the external surface sites of the sorbent, where the associated energy levels vary depending on the nature of the interaction (physical or chemical); and (iii) diffusion of MB molecules into the interior adsorption sites of the sorbent via intraparticle or solid-state diffusion mechanisms. The intraparticle diffusion parameters for the adsorption of MB are outlined in Table 3. In any adsorption process, the overall rate-controlling step may involve one or a combination of these stages.

Table 3. Intraparticle diffusion parameters for the adsorption of MB.

C_0 (mg L^{-1})	ki (mg g^{-1} $s^{-1/2}$)	C (mg g^{-1})	R^2
4	–0.0143	1.0425	0.8872
8	–0.0254	1.4996	0.8165
12	–0.0426	1.7251	0.8023
16	–0.0276	1.1698	0.8301
20	–0.0286	1.2316	0.8260

C_0 = initial methylene blue (MB) concentration; k_i = intraparticle diffusion rate constant; C = intercept related to the boundary layer thickness; R^2 = coefficient of determination.

The intraparticle diffusion model is expressed as Eqn. 8:

$$q_t = K_{id} t^{1/2} + C \tag{8}$$

where

C is the intercept related to boundary layer thickness, and

k_{id} is the intraparticle diffusion rate constant.

3.3.4 Thermodynamic Studies

Thermodynamic equations were employed to analyse the thermodynamic behaviour of the adsorption process. This approach helps to elucidate the overall adsorption mechanism and the associated changes in energy during the process. The following thermodynamic models were applied to determine the parameters used in the present investigation, including the standard Gibbs free energy change (ΔG^0), enthalpy change (ΔH^0), and entropy change (ΔS^0) (Eqns. 9,10,11):

$$K_{id} = \frac{q_e}{C_e} \tag{9}$$

$$\Delta G^0 = -RTlnK_{id} \tag{10}$$

$$lnK_{id} = \frac{\Delta S^0}{R} - \frac{\Delta H^0}{RT} \tag{11}$$

where

T is the absolute temperature (K),

R is the universal gas constant (8.3145 J mol^{-1} K^{-1}), and

K_{id} is the distribution coefficient.

Thermodynamic parameters (ΔG^0, ΔH^0, and ΔS^0) were determined using the Van't Hoff plot obtained from the linear regression of ln (K_{id}) versus 1/temperature, (1/T (K^{-1})). The calculated thermodynamic parameters are summarised in Table 4. The negative ΔG^0 values indicate that the adsorption process is spontaneous, with increasingly negative values corresponding to higher dye uptake.

The positive ΔS^0 values suggest an increase in randomness at the solid–solution interface and indicate a strong affinity of MB towards BPMNC beads during adsorption. Supporting evidence from SEM and FTIR analyses reveals distinct structural and chemical changes in the beads before and after adsorption. In addition, TGA results confirm the good thermal stability of the biopolymer-based nanocomposite. Furthermore, the pH study revealed that pH 6 is operationally optimal for MB adsorption. The Langmuir isotherm model provided a better fit than the Freundlich model, and the Freundlich constant (*n*) fell within the range associated with favourable endothermic adsorption. Thus, the evaluated thermodynamic, kinetic, and isotherm parameters confirm a strong tendency of the MB dye to adsorb onto BPMNC beads. A detailed description of the experimental conditions, optimization, and supporting spectroscopic and structural analyses, including UV–Vis, FTIR, and XRD, is presented in the **Supplementary Material** section (**Supplementary Figs. 1–5**).

4. Discussion

4.1 Proposed Adsorption Mechanism of BPMNC

The adsorption performance of the BPMNC is governed by a synergistic combination of physicochemical interactions, as shown in Fig. 24. The presence of multiple surface functional groups (–OH and $–COO^-$) within the biopolymer matrix, together with uniformly distributed Zn^{2+}, Co^{2+}, Fe^{3+}, and Ca^{2+} ions, provides abundant active sites for adsorption. Electrostatic attraction between the charged surface sites and the adsorbate molecules plays a crucial role during the initial stage of adsorption.

Surface complexation, resulting from the coordination of metal ions with electron-donating functional groups, enhances adsorption stability. In addition, π–π interactions between aromatic structures of the adsorbate and the composite matrix, along with hydrogen bonding involving –OH and –COOH groups, further strengthen the adsorption process. The porous structure of the nanocomposite facilitates

Table 4. Thermodynamic parameters for the adsorption of MB.

T (°C)	T (K)	ΔG^0 (KJ/mol)	ΔH^0 (KJ/mol)	ΔS^0 (J/mol/K)
30	303	–13.54	0.08	44.96
40	313	–14.00	0.08	44.96
50	323	–14.46	0.08	44.96
60	333	–14.92	0.08	44.96
70	343	–15.38	0.08	44.96

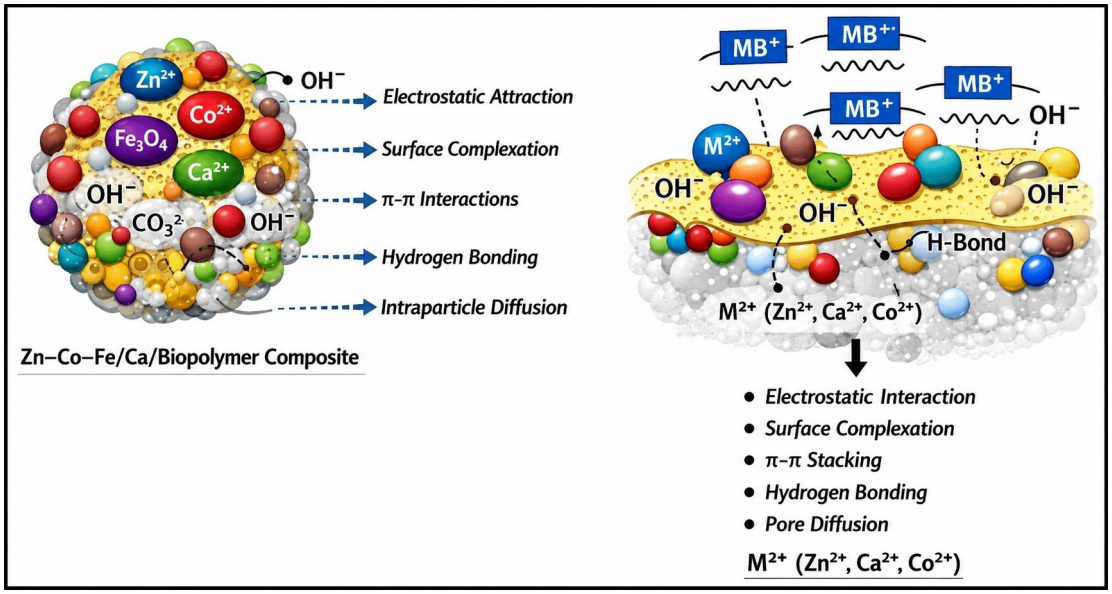

Fig. 24. Adsorption mechanism of the proposed adsorbent material.

efficient pore and intraparticle diffusion, allowing adsorbate molecules to access internal active sites and sustain adsorption at later stages. Thus, the coexistence of electrostatic interaction, surface complexation, π–π stacking, hydrogen bonding, and diffusion processes accounts for the high adsorption capacity and robust adsorption behaviour of the proposed adsorbent material.

4.2 Structure-Performance Relationship of Biopolymer Nanocomposite

The structure–performance relationship of the BPMNC is clearly shown in Fig. 25 by correlating FTIR and SEM characterisation with the adsorption mechanism and adsorption performance. FTIR analysis confirms the presence of abundant surface functional groups, including –OH and $–COO^-$, and their interaction with Zn^{2+}, Co^{2+}, Ce^{3+}/Ce^{4+}, and Ca^{2+} ions, indicating successful metal incorporation and the availability of active binding sites for adsorption. SEM micrographs reveal a heterogeneous, rough, and porous surface morphology, which enhances the surface area and facilitates accessibility of adsorbate molecules to internal active sites. These structural features directly govern the adsorption mechanism, which involves synergistic electrostatic interactions, surface complexation between metal ions and functional groups, π–π interactions (for aromatic adsorbates), hydrogen bonding, and efficient pore and intraparticle diffusion. As a consequence of this optimised structure and multifunctional interaction pathway, the nanocomposite exhibits superior adsorption performance, characterised by high adsorption capacity, pseudo-second-order kinetic behaviour indicative of chemisorption-dominated processes, and monolayer adsorption consistent with the Langmuir isotherm model. In summary, the strong correlation between the chemically active surface (FTIR), favourable morphology (SEM), and multimechanistic adsorption behaviour explains the enhanced adsorption efficiency and stability of the proposed adsorbent material.

4.3 Reusability Studies

Reusability tests demonstrate minimal loss in adsorption efficiency over multiple cycles. The reusability performance of BPMNC for MB adsorption, as summarised in Fig. 26, confirms the economic feasibility of BPMNC and demonstrates strong potential for repeated wastewater treatment applications. The reusability of the adsorbent nanocomposite was evaluated over multiple adsorption-desorption cycles to assess its operational stability and economic feasibility. The BPMNC exhibited high regeneration efficiency, retaining approximately 90% of its initial MB removal capacity after five consecutive cycles under optimised conditions. The marginal decline in adsorption

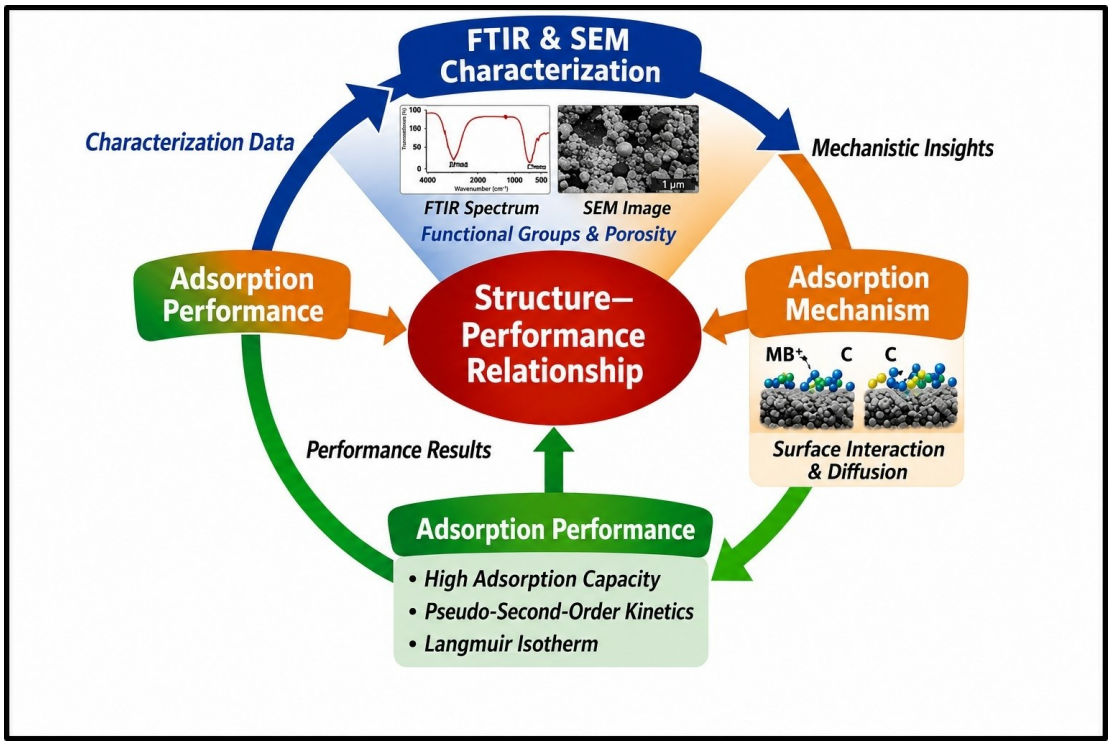

Fig. 25. The structure performance relationship.

performance can be attributed to partial blockage of active sites and incomplete desorption of dye molecules during regeneration.

Despite repeated use, the maintained adsorption efficiency highlights the strong structural integrity of the calcium-crosslinked biopolymer matrix, ensuring effective stabilisation of the embedded multi-metal active sites and minimal nanoparticle leaching. The preservation of adsorption capacity across repeated cycles further indicates that the dominant chemisorption mechanism and synergistic metal-dye interactions remain largely unaffected by regeneration treatment. The excellent reusability performance demonstrates that BPMNC is a robust and cost-effective adsorbent, reinforcing its suitability for practical and sustainable dye-laden wastewater treatment applications.

4.4 Comparative Evaluation With Reported Adsorbents

The comparative performance of different adsorbent materials, including the developed adsorbent, is summarised in Table 5 (Ref. [38,39,40,41,42]). Figs. 27,28 present a comparative analysis of MB removal efficiency and important operational parameters for various adsorbents, highlighting the enhanced performance of the Zn-Co-Fe/Ca biopolymer nanocomposite BPMNC, which achieves 97% removal at a near-neutral pH of 6. BPMNC demonstrates high adsorption efficiency at a moderate adsorbent dose of 1 g, a short contact time of 60 min, and an initial MB concentration of 12 mg L^{-1}, outperforming many reported adsorbents that require extreme pH conditions, higher dosages, or prolonged treatment times. XRD and XPS analyses confirmed the presence of stable crystalline spinel phases with heterogeneous surface charges arising from multiple metal oxidation states. BET analysis further revealed a mesoporous structure that facilitates rapid dye diffusion and enhances site accessibility. The adsorption data were best fitted by the Langmuir isotherm and pseudo-second-order kinetic models, suggesting a monolayer chemisorption process dominated by strong dye–surface interactions. The adsorption mechanism involves synergistic electrostatic attraction, hydrogen bonding, π–π interactions, and metal–dye complexation, while the Ca-crosslinked biopolymer matrix prevents nanoparticle agglomeration, thereby ensuring structural stability. Reusability studies demonstrate excellent regeneration potential, with negligible performance loss over multiple cycles, establishing BPMNC as a practically viable and superior adsorbent for dye-laden wastewater treatment relative to previously reported materials.

4.5 Limitations of the Study

Despite the encouraging adsorption performance of the developed adsorbent material, a few limitations were identified. The study focused exclusively on MB as a model cationic dye, and the adsorption behaviour of anionic, non-ionic, or mixed dye systems was not evaluated. Furthermore, all experiments were conducted using synthetic aqueous solutions; therefore, the influence of competing ions and organic matter commonly present in actual industrial effluents remains unexplored. The adsorption performance was assessed through batch experiments, while continuous-

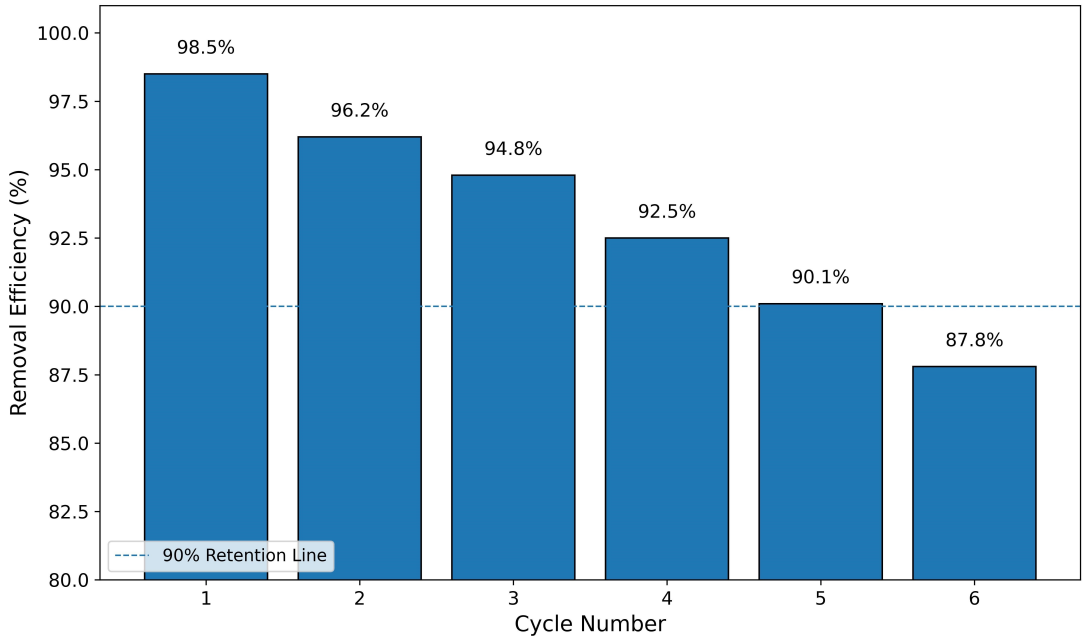

Fig. 26. Reusability performance of BPMNC for MB adsorption.

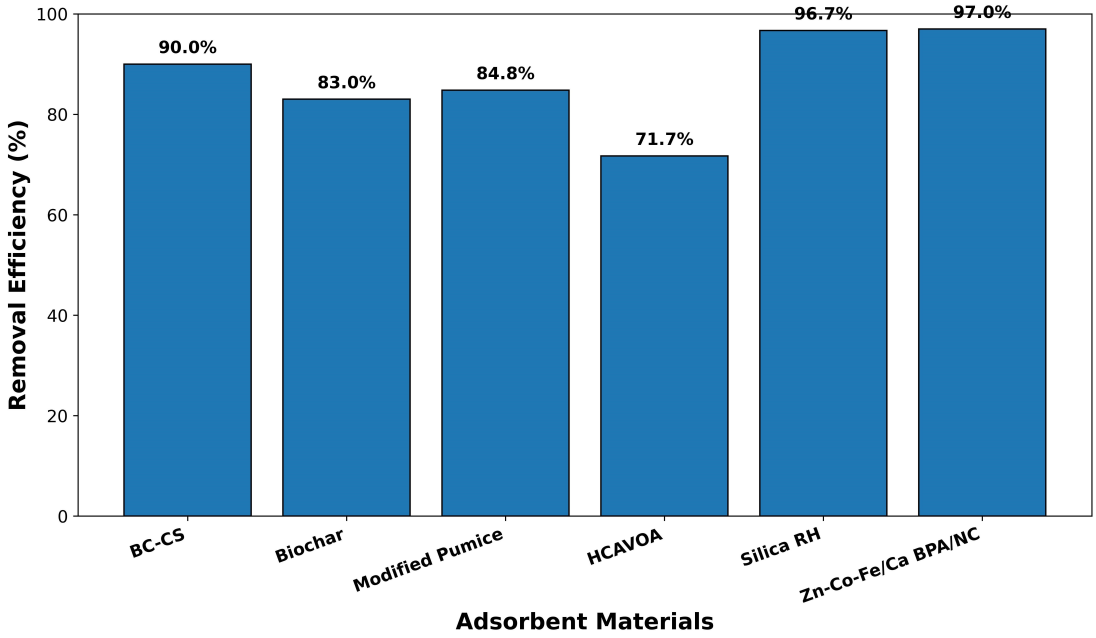

Fig. 27. Comparative advantage of adsorbent material: MB removal efficiency of various adsorbents.

flow or column studies were not conducted. Such investigations are required to evaluate mass transfer effects, operational stability, and scalability. Regeneration studies were limited to a small number of cycles, and long-term stability, potential nanoparticle leaching, and cost-effectiveness were not examined. Addressing these limitations in future studies will be essential to confirm the practical applicability of BPMNC for large-scale wastewater treatment.

5. Conclusions

The study establishes a highly efficient BPMNC for the effective removal of MB from aqueous solutions. The synergistic integration of transition metals Zn, Co, and Fe with alkaline earth metal Ca within a biopolymer matrix significantly enhanced adsorption capacity, structural stability, and environmental compatibility compared with conventional single or binary metal adsorbents. Comprehensive physicochemical characterisation using FTIR,

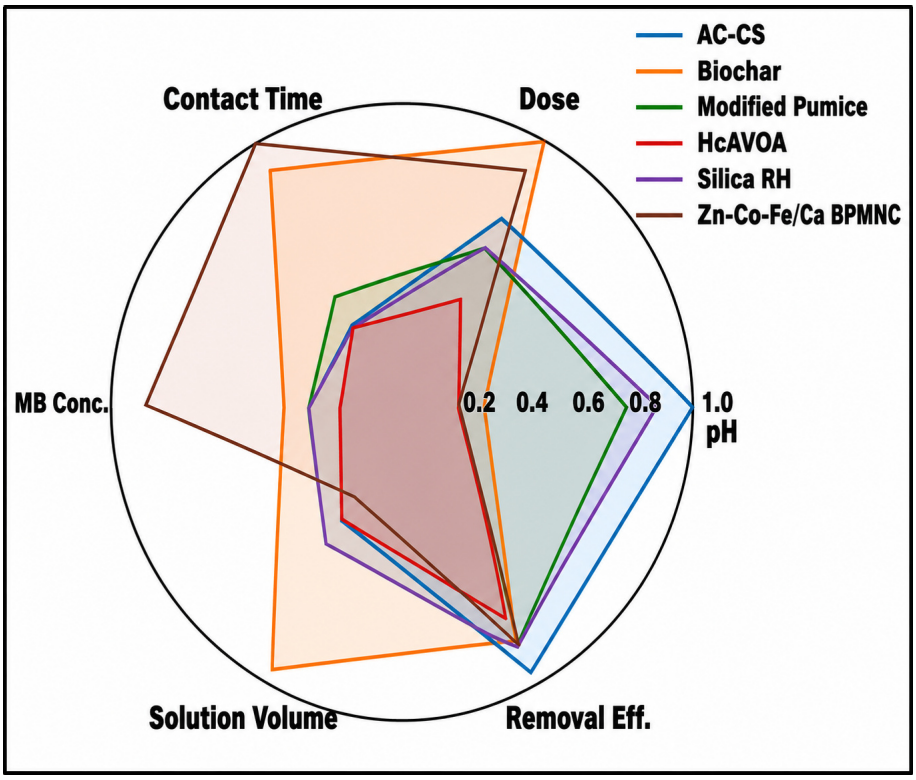

Fig. 28. Comparative advantage of adsorbent material: Normalised multi-parameter comparison of adsorbents.

Table 5. Comparison of developed biopolymer composite with other adsorbents for MB removal.

Adsorbent material	Max. removal efficiency (%)	Experimental conditions	Reference
Activated carbon from corn stalk (AC–CS)	90	pH 11; adsorbent dose 1.4 g L^{-1}; contact time 50 min; MB concentration 10 mg L^{-1}; temperature 25 ± 2 °C; solution volume 100 mL	[38]
Biochar from hazelnut shells	83	pH 4.0; adsorbent dose 1.5 g L^{-1}; contact time 300 min; MB concentration 15 mg L^{-1}; temperature 45 °C; agitation speed 150 rpm; solution volume 250 mL	[39]
Modified pumice stone	84.8	pH 10; adsorbent dose 0.2 g L^{-1}; contact time 120 min; MB concentration 30 mg L^{-1}; solution volume 50 mL	[40]
$HoCaWO_4$ nanoparticles	71.17	pH 2.03; adsorbent dose 1.91 g L^{-1}; contact time 15.16 min; MB concentration 100.65 mg L^{-1}; agitation speed 180 rpm; temperature 25 ± 2 °C; solution volume 100 mL	[41]
Silica from raw rice husk	96.7	pH 8; adsorbent dose 1 g L^{-1}; contact time 60 min; MB concentration 10 mg L^{-1}; solution volume 100 mL	[42]
Zn-Co-Fe/Ca biopolymer nanocomposite	97	pH 6; adsorbent dose 1 g; contact time 60 min; MB concentration 12 mg L^{-1}; temperature 40 °C; solution volume 50 mL	This study

SEM, XRD, XPS, BET, TGA, and pH_pzc confirmed the effective immobilisation of metal species, mesoporous surface characteristics, and strong dye–surface interactions. Adsorption experiments demonstrated optimal operational performance at near-neutral pH 6, achieving rapid uptake within 60 minutes using a moderate adsorbent dosage, while maintaining high removal efficiency even at elevated dye concentrations. Higher removal efficiencies were observed at an optimum pH of 6 and a temperature of 40°C, while prolonged contact time and increased adsorbent dosage further enhanced the adsorption performance. Kinetic and isotherm analyses indicated pseudo-second-order behaviour and Langmuir-type monolayer adsorption, confirming chemisorption-dominated uptake on energetically uniform sites. Thermodynamic evaluation confirmed the spontaneous and endothermic nature of the adsorption process, indicating a strong affinity between MB molecules and the nanocomposite surface. The adsorption mecha-

nism involved synergistic electrostatic attraction, hydrogen bonding, π–π interactions, and metal–dye complexation, supported by a stable Ca-cross-linked biopolymer framework, which effectively suppressed nanoparticle agglomeration. In addition, the nanocomposite exhibited excellent regeneration capability with negligible loss in performance over multiple cycles, highlighting its economic feasibility and reusability. Collectively, this study establishes the proposed adsorbent as a practical, scalable solution for dye-laden wastewater, demonstrating significant potential for industrial-scale applications and the treatment of real wastewater effluents.

Availability of Data and Materials

The datasets generated and analyzed during the current research are openly available in the GitHub repository: https://github.com/team2425/ABPBAM. Researchers can access and download the complete dataset, explore sample formats, and utilize the provided code for replication and further analysis. Any updates to the data or additional supporting files will be maintained at the above link to ensure transparency and reproducibility of the research findings.

Author Contributions

SPMJ carried out the experimental investigations, data analysis, and manuscript drafting. JD conceived the study, provided supervision and guidance, reviewed and edited the manuscript. Both authors read and approved the final manuscript. Both authors have participated sufficiently in the work and agreed to be accountable for all aspects of the work.

Ethics Approval and Consent to Participate

Not applicable.

Acknowledgment

The authors gratefully acknowledge the laboratory facilities and technical support provided by the Centre for Nanoscience and Technology, Anna University, Chennai–600025, Tamil Nadu, India.

Funding

This research received no external funding.

Conflicts of Interest

The authors declare no conflicts of interest.

Supplementary Material

Supplementary material associated with this article can be found, in the online version, at https://doi.org/10.31083/DJNB55237.

References

[1] Kayani KF, Mohammed SJ, Mustafa MS, Aziz SB. Dyes and their toxicity: Removal from wastewater using carbon dots, metal oxides as hybrid materials: A review. Materials Advances. 2025; 6: 5391–5409. https://doi.org/10.1039/D5MA00572H

[2] Kayani KF. Bimetallic metal-organic frameworks (BMOFs) for dye removal: a review. RSC Advances. 2024; 14: 31777–31796. https://doi.org/10.1039/d4ra06626j

[3] Uddin F. Environmental hazard in textile dyeing wastewater from the local textile industry. Cellulose. 2021; 28: 10715–10739. https://doi.org/10.1007/s10570-021-04228-4

[4] Pereira L, Alves M. Dyes: environmental impact and remediation. In Malik A, Grohmann E (eds.) Environmental Protection Strategies for Sustainable Development. Strategies for Sustainability (pp. 111–162). Springer: Dordrecht. 2012.

[5] Nidheesh PV, Gokkus O. Aerated iron electrocoagulation process as an emerging treatment method for natural water and wastewater. Separation Science and Technology. 2023; 58: 2041–2063. https://doi.org/10.1080/01496395.2023.2227913

[6] Wante HP, Yap SL, Khan AA, Chowdhury ZZ, Nee CH, Yap SS, et al. Enhanced adsorption of malachite green dye using plasma-modified coconut carbon shell. Diamond and Related Materials. 2024; 149: 111650. https://doi.org/10.1016/j.diamond.2024.111650

[7] Dutta S, Adhikary S, Bhattacharya S, Roy D, Chatterjee S, Chakraborty A, et al. Contamination of textile dyes in aquatic environment: Adverse impacts on aquatic ecosystem and human health, and its management using bioremediation. Journal of Environmental Management. 2024; 353: 120103. https://doi.org/10.1016/j.jenvman.2024.120103

[8] Periyasamy AP. Textile dyes in wastewater and their impact on humans and the environment. Focus on bioremediation. Water, Air, Soil, and Pollution. 2025; 236: 562. https://doi.org/10.1007/s11270-025-08204-7

[9] Lin J, Ye W, Xie M, Seo DH, Luo J, Wan Y, et al. Environmental impacts and remediation of dye-containing wastewater. Nature Reviews Earth and Environment. 2023; 4: 785–803. https://doi.org/10.1038/s43017-023-00489-8

[10] Rorissa GL, Tesema EA, D M RP, Hunde AR, Beyena SY, Biru MA, et al. Removal of methylene blue dye from textile industry wastewater using green synthesized Teff straw assisted ZnO nanoparticle. Scientific Reports. 2025; 15: 26230. https://doi.org/10.1038/s41598-025-11746-9

[11] Goutam SP, Saxena G, Roy D, Yadav AK, Bharagava RN. Green synthesis of nanoparticles and their applications in water and wastewater treatment. In Saxena G, Bharagava R (eds.) Bioremediation of Industrial Waste for Environmental Safety. Springer: Singapore. 2020.

[12] Ahmadi S, Igwegbe CA. Removal of methylene blue on zinc oxide nanoparticles: Adsorption isotherm and kinetic study. Sigma Journal of Engineering and Natural Sciences. 2020; 1: 289–303.

[13] Amin MT, Alazba AA, Shafiq M. Effective adsorption of methylene blue using activated carbon from rosemary plant. Desalination and Water Treatment. 2017; 74: 336–345. https://doi.org/10.5004/dwt.2017.20572

[14] Dod R, Banerjee G, Saini S. Adsorption of methylene blue using green pea peels. Biotechnology and Bioprocess Engineering. 2012; 17: 862–874. https://doi.org/10.1007/s12257-011-0614-5

[15] Peighambardoust SJ, Rezaei-Aghdam S, Sakhaei Niroumand J, Mohammadzadeh Pakdel P, Sillanpää M. Efficient methylene blue elimination from water media by nanocomposite adsorbent-based carboxymethyl cellulose-grafted poly(acrylamide)/magnetic biochar decorated with ZIF-67. RSC Advances. 2025; 15: 32407–32423. https://doi.org/10.1039/d5ra03796d

[16] Oladoye PO, Ajiboye TO, Omotola EO, Oyewola OJ. Methylene blue toxicity and removal technologies. Results in Engineer-

ing. 2022; 16: 100678. https://doi.org/10.1016/j.rineng.2022.100678
[17] Crini G, Lichtfouse E. Advantages and disadvantages of wastewater treatment techniques. Environmental Chemistry Letters. 2019; 17: 145–155. https://doi.org/10.1007/s10311-018-0785-9
[18] Bhatnagar A, Sillanpaa M. Utilisation of waste materials as adsorbents for water treatment. Chemical Engineering Journal. 2010; 157: 277–296. https://doi.org/10.1016/j.cej.2010.01.007
[19] Cui C, Li D, Wang LJ. Functionalized nanocomposite biopolymer-based environmental-friendly adsorbents: Design, adsorption mechanism, regeneration, and degradation. Separation and Purification Technology. 2025; 363 (Part 1): 132034. https://doi.org/10.1016/j.seppur.2025.132034
[20] Ahmed MJ, Hameed BH, Hummadi EH. Review on recent progress in chitosan/chitin-carbonaceous material composites for the adsorption of water pollutants. Carbohydrate Polymers. 2020; 247: 116690. https://doi.org/10.1016/j.carbpol.2020.116690
[21] Ngah WSW, Teong LC, Hanafiah MAKM. Adsorption of dyes and heavy metals by chitosan composites. Carbohydrate Polymers. 2011; 83: 1446–1456. https://doi.org/10.1016/j.carbpol.2010.11.004
[22] Wang B, Wan Y, Zheng Y, Lee X, Liu T, Yu Z, et al. Alginate-based composites for environmental applications: A critical review. Critical Reviews in Environmental Science and Technology. 2018; 49: 318–356. https://doi.org/10.1080/10643389.2018.1547621
[23] Mohanrasu K, Manivannan AC, Rengarajan HJR, Kandaiah R, Ravindran A, Panneerselvan L, et al. Eco-friendly biopolymers and composites for pollutant removal. Materials Sustainability. 2025; 3: 13. https://doi.org/10.1038/s44296-025-00057-9
[24] Danyliuk I. Biopolymer-based metal oxide nanoparticles for water treatment. In Fesenko O, Yatsenko L (eds.) Nanoengineering, Nanobiotechnology, Nanochemistry, and Their Applications. Springer: Cham, Switzerland. 2026.
[25] Ganesh A, Rajan R, Mathew Simon S, Thankachan S. Metal oxide incorporated bionanocomposites and applications. Nano Structures and Nano Objects. 2024; 38: 101126. https://doi.org/10.1016/j.nanoso.2024.101126
[26] Malik R, Nazreen, Meena J. Copper oxide biopolymer nanocomposites: A review. Vietnam Journal of Science and Technology. 2024; 62: 836–858. https://doi.org/10.15625/2525-2518/20843
[27] Saini S, Saini T, Verma V, Meena J. Biopolymer-based nanocomposites reinforced with metallic nanoparticles. Acta Biology Forum. 2024; 4: 06–15. https://doi.org/10.51470/ABF.2024.4.2.06
[28] Basavegowda N, Baek KH. Advances of Metal and Metal Oxide Nanocomposites. MDPI: Basel, Switzerland. 2023.
[29] Verma DK, Malik R, Meena J, Rameshwari R. Chitosan-based metallic nanoparticles: A review. Journal of Applied and Natural Science. 2021; 13: 544–551. https://doi.org/10.31018/jans.v13i2.2635
[30] Dhila H, Bhapkar A, Bhame S. Metal oxide biochar hybrid nanocomposites for dye remediation. Desalination and Water Treatment. 2025; 321: 101004. https://doi.org/10.1016/j.dwt.2025.101004
[31] AbdElhady MM. Preparation and characterisation of chitosan zinc oxide nanoparticles. International Journal of Carbohydrate Chemistry. 2012; 2012: 840591. https://doi.org/10.1155/2012/840591
[32] Alam A, Hassan A, Sultana Z, Das N. Natural polymer-based bioadsorbents for wastewater treatment. RSC Sustainability. 2025; 3: 5027–5046. https://doi.org/10.1039/D5SU00369E
[33] Lanjwani MF, Tuzen M, Khuhawar MY, Saleh TA. Photocatalytic degradation of organic dyes using nanoparticles. Inorganic Chemistry Communications. 2024; 159: 111613. https://doi.org/10.1016/j.inoche.2023.111613
[34] Borpujari P, Khan S, Dutta J, Borah D. Biochar metal nanocomposites for azo dye removal. Discover Applied Sciences. 2025; 7: 1023. https://doi.org/10.1007/s42452-025-07706-7
[35] Al-Gethami W, Qamar MA, Shariq M, Alaghaz ANMA, Farhan A, Areshi AA, et al. Emerging environmentally friendly bio-based nanocomposites for the efficient removal of dyes and micropollutants from wastewater by adsorption: a comprehensive review. RSC Advances. 2024; 14: 2804–2834. https://doi.org/10.1039/d3ra06501d
[36] Vaidyanathan G, Sendhilnathan S. Synthesis and characterisation of spinel ferrite nanoparticles. Journal of Magnetism and Magnetic Materials. 2008; 320: 803–809.
[37] Lagergren S. Zur Theorie der sogenannten Adsorption gelöster Stoffe [On the theory of so-called adsorption of dissolved substances]. Kungliga Svenska Vetenskapsakademiens Handlingar. 1898; 24: 1–39. (In German)
[38] Nayeri D, Mousavi SA, Fatahi M, Almasi A, Khodadoost F. Dataset on adsorption of methylene blue from aqueous solution onto activated carbon obtained from low cost wastes by chemical-thermal activation - modelling using response surface methodology. Data in Brief. 2019; 25: 104036. https://doi.org/10.1016/j.dib.2019.104036
[39] Kaya N, Yildiz Z, Ceylan S. Biochar from hazelnut shell for methylene blue adsorption. Politeknik Dergisi. 2018; 21: 765–776. https://doi.org/10.2339/politeknik.386963
[40] Derakhshan Z, Baghapour MA, Ranjbar M, Faramarzian M. Adsorption of methylene blue using modified pumice stone. Health Scope. 2013; 2: 136–144. https://doi.org/10.17795/jhealthscope-12492
[41] Igwegbe CA, Mohmmadi L, Ahmadi S, Rahdar A, Khadkhodaiy D, Dehghani R, et al. Modeling of adsorption of Methylene Blue dye on Ho-$CaWO_4$ nanoparticles using Response Surface Methodology (RSM) and Artificial Neural Network (ANN) techniques. MethodsX. 2019; 6: 1779–1797. https://doi.org/10.1016/j.mex.2019.07.016
[42] Moeinian K, Mehdinia SM. Removing methylene blue using rice husk silica adsorbent. Polish Journal of Environmental Studies. 2019; 28: 2281–2287. https://doi.org/10.15244/pjoes/91044